REPORT DOCUMENTATION PAGE	*Form Approved* *OMB No. 0704-0188*

1. REPORT DATE *(DD-MM-YYYY)* 14-05-2008	**2. REPORT TYPE** Final Report	**3. DATES COVERED** *(From - To)* 2/15/07 - 2/14/08

4. TITLE AND SUBTITLE
Pre-Flight Ground Testing of the Full-Scale HIFiRE-1 Vehicle at Fully Duplicated Flight Conditions: Part II

5a. CONTRACT NUMBER

5b. GRANT NUMBER
FA9550-07-1-0486

5c. PROGRAM ELEMENT NUMBER

6. AUTHOR(S)
Wadhams, Tim, P.
Mundy, Erik
MacLean, Matthew, G.
Holden, Michael, S.

5d. PROJECT NUMBER

5e. TASK NUMBER

5f. WORK UNIT NUMBER

7. PERFORMING ORGANIZATION NAME(S) AND ADDRESS(ES)
CUBRC, Inc.
4455 Genesee Street
Buffalo, NY 14225

8. PERFORMING ORGANIZATION REPORT NUMBER

9. SPONSORING/MONITORING AGENCY NAME(S) AND ADDRESS(ES)
AF OFFICE OF SCIENTIFIC RESEARCH
875 N. RANDOLPH ST. ROOM 3112
ARLINGTON VA 22203

10. SPONSOR/MONITOR'S ACRONYM(S)
AFRL, AFOSR

11. SPONSOR/MONITOR'S REPORT NUMBER(S)
AFRL-AFOSR-VA-TR-2016-0691

12. DISTRIBUTION/AVAILABILITY STATEMENT
Approved for public release; distribution is unlimited.

13. SUPPLEMENTARY NOTES

14. ABSTRACT

As part of a two phase experimental study to obtain detailed heating and pressure data over the full-scale HIFiRE (formally FRESH FX-1) flight geometry, CUBRC has completed a matrix of ground tests to determine the optimal flight geometry and instrumentation configuration necessary to make measurements of desired flow phenomena during the flight experiment. The primary objective of the HIFiRE (Hypersonic International Flight Research and Experimentation) flight experiment is to collect high quality flight data from integrated flight instrumentation to be used for CFD code and ground test facility validation in regions of boundary layer transition, turbulent separated flow, and shock-boundary layer interaction. To support this flight experiment, data has been obtained in the LENS I hypervelocity wind tunnel employing a full-scale model over a range of Mach numbers from 6.5 to 7.4, and Reynolds numbers of 0.5E+06 to 5.5E+6 duplicating the reentry trajectory. These points gave researchers the best chance to measure the transition process on the fore cone and have a turbulent separated flow on the cylinder that reattached onto the flare section.

15. SUBJECT TERMS
HIFiRE-1, Flight Experiment, Boundary Layer Transition, Turbulent Shock/Boundary Layer Interaction

16. SECURITY CLASSIFICATION OF:			**17. LIMITATION OF ABSTRACT**	**18. NUMBER OF PAGES**	**19a. NAME OF RESPONSIBLE PERSON**
a. REPORT	**b. ABSTRACT**	**c. THIS PAGE**			Timothy P. Wadhams
Unclassified	Unclassified	Unclassified	UU	33	**19b. TELEPHONE NUMBER** *(Include area code)* 716-204-5125

Pre-Flight Ground Testing of the Full-Scale HIFiRE-1 Vehicle at Fully Duplicated Flight Conditions: Part II

T.P. Wadhams[*], E. Mundy[†],
M.G. MacLean[‡], M.S. Holden[§]
CUBRC, Buffalo, New York 14225

Abstract

As part of a two phase experimental study to obtain detailed heating and pressure data over the full-scale HIFiRE (formally FRESH FX-1) flight geometry, CUBRC has completed a matrix of ground tests to determine the optimal flight geometry and instrumentation configuration necessary to make measurements of desired flow phenomena during the flight experiment. The primary objective of the HIFiRE (Hypersonic International Flight Research and Experimentation) flight experiment is to collect high quality flight data from integrated flight instrumentation to be used for CFD code and ground test facility validation in regions of boundary layer transition, turbulent separated flow, and shock-boundary layer interaction. To support this flight experiment, data has been obtained in the LENS I hypervelocity wind tunnel employing a full-scale model over a range of Mach numbers from 6.5 to 7.4, and Reynolds numbers of 0.5E+06 to 5.5E+6 duplicating the reentry trajectory. These points gave researchers the best chance to measure the transition process on the fore cone and have a turbulent separated flow on the cylinder that reattached onto the flare section. These test condition ranges were determined directly from the nominal decent trajectory of the Australian launched Terrier-Orion launch vehicle that will serve as the booster for HIFiRE. The program was completed in two distinct phases. The first phase consisted of a geometry study to aid in the selection of the proper nose radius to achieve the desired transition location on the fore cone, and to establish the flare angle necessary to achieve a turbulent separation zone with reattachment back onto the flare. The first phase also established locations where additional instrumentation should be added for high fidelity testing in the second phase that would be used to compare to the flight data and for validating computational methods. This current paper will briefly review the first phase results, but will be primarily concerned with the results of the second phase of the program. The objectives of the second phase consisted of obtaining additional detailed heat transfer and pressure data in the transition region on the forecone and in the interaction region around the cylinder/flare junction for a range of Reynolds numbers and model attitudes. The number of heat transfer sensors has been more than doubled in these regions from the first phase to obtain higher resolution information concerning the transition process and interaction region. New to this phase was testing with a discreet diamond shape roughness element that will be employed in flight to allow a greater portion of the flight trajectory to produce turbulent flow over the vehicle. This roughness element will be placed on one side only and testing was done in LENS I to examine the effect of the roughness over this trajectory range. The entire experimental database will be used to compare to the future flight data and by computationalists to validate codes in regions of attached and separated laminar and turbulent flows with shock/boundary layer interaction. In addition to the experimental data, CUBRC also performed a large amount of CFD analysis to confirm and validate not only the tunnel flow conditions, but also 2D and 3D flows over the model itself.

---

[*] Research Scientist, AAEC, CUBRC, 4455 Genesee Street, Buffalo, NY.

[†] Research Engineer, AAEC, CUBRC, 4455 Genesee Street, Buffalo, NY.

[‡] Senior Research Scientist, AAEC, CUBRC, 4455 Genesee Street, Buffalo, NY.

[§] Program Manager, AAEC, CUBRC, 4455 Genesee Street, Buffalo, NY.

Experimental work and analysis performed during this program was supported and directed under contract to the Air Force Office of Scientific Research (AFOSR) and Air Force Research Laboratory (AFRL).

I. Introduction and Program Overview

Over the past year, experimental and computational studies have been conducted in two distinct phases by the CUBRC Aerothermal Aero-optic Evaluation Center (AAEC) team to assist in the selection of a blunted cone/cylinder/flare configuration to be employed in the AFOSR/AFRL-sponsored HIFiRE FRESH FX-1 flight test program. FRESH FX-1 stands for Fundamental RESearch in Hypersonics Flight eXperiments and the objective of the first phase of the ground test program was to select nosetip and flare geometries that give researchers the best chance to obtain boundary layer transition, turbulent separated flow, and shock wave/boundary layer interaction data in flight. The ground test and flight results will represent an important database to evaluate the prediction methods that describe these classes of hypersonic flows. CUBRC's LENS I hypervelocity shock tunnel was selected to meet these objectives because of the facility's capability to duplicate the required freestream conditions while testing a full-scale version of the flight vehicle. Freestream conditions for these studies were selected from the trajectory of the Australian Terrier-Orion booster, the launch vehicle for the flight test, at points where transition would occur in a desirable location on the cone. Angle of attack measurements were also obtained as they pertain to the expected trajectory to explore the three-dimensional transition and shock/wave turbulent boundary layer interaction effects the vehicle will experience in flight. Additionally high-speed schlieren movies were taken of the flare region to assess separated region length for variations in flare angle, freestream condition, and model attitude. The flare was not instrumented in this first phase of the program to allow the geometry, specifically the angle, to be changed with minimal downtime between tests. The first phase experiments resulted in a blunt 2.5-millimeter nose and flare angle of 33°, which will be the eventual flight geometry.

The second phase of the ground test program, which is described in detail in this paper, was designed to obtain additional higher resolution data in the transition region, to obtain pressure and heat flux data in the flow separation/interaction region over the flare, and to study the effects of a discreet diamond roughness element on the transition process. The heat flux results and high-speed schlieren video from the first phase were directly employed to place the additional instruments. These additional heat flux instruments more than doubled the number of heat flux sensors and represented sufficient resolution for code validation efforts. The first several experiments were performed duplicating conditions and model geometry from the first phase to verify that new results compared favorably to those already obtained. These tests showed that while the data on the cone and cylinder sections agreed with the results from the first entry the flare results showed that for the flight flare length the data lacked an appreciable plateau region behind the interaction peak to be used as a boundary condition for computationalists. An extended length flare was constructed and the test program proceeded normally obtaining a dataset capable validating computational methods and comparing to the flight results. The second phase of the ground test also included the addition of a diamond roughness element to the cone surface. This trip was designed to extend the duration of the flight test where turbulent results can be obtained. The flight test plan calls for the trip to be placed on only one side of the flight vehicle and hence only produce turbulent flow on that side with laminar or smooth body transition on the other side. This flight state required ground testing to verify that the effects of the trip did not feed to the other side of the model over a range of Reynolds numbers and model attitudes. Secondary objectives of the experimental study included obtaining detailed high-speed schlieren movies of the boundary layer transition on the cone, employing time of arrival pressure transducers to obtain 2nd mode transition frequencies, and making pitot pressure measurements to characterize the level and frequency of the fluctuating pressure component due to the turbulent boundary layer on the facility nozzle wall.

In a similar fashion to what was done in the first phase CUBRC also performed a large amount of computational work assessing both the flow in the test facility and the freestream flow over the model. These computational results include laminar and turbulent predictions of pressure and heat transfer on the cone and cylinder sections employing the DPLR code, and stability calculations of the forebody utilizing STABL. New to this phase is an assessment of turbulence models and the prediction of turbulent flow in regions of separation, reattachment, and shock/boundary layer interaction. This work will be briefly mentioned here but will be described in detail in Reference 1 [MacLean 2008]. Finally new e^N method STABL calculations will be made with the additional heat flux instrumentation results to assess if this higher resolution dataset has an influence on the interpretation of laminar-turbulent transition onset.

II. Facilities and Instrumentation

A. The LENS Facility

The aerothermal tests in this program were performed in the LENS I hypervelocity reflected shock tunnel. A schematic diagram of the LENS I HST is shown alongside the LENS II and LENS X facilities in Figure 1. The three facilities share a common control system, compressor system, data recording system and data analysis system. LENS I has the capability to fully duplicate flight conditions at Mach numbers ranging from 6 to 15, while LENS II has similar capabilities from Mach 3 to 7. The major components of the LENS I facility include a 25.5-foot long by 11-inch diameter electrically heated driver tube, a double diaphragm assembly, a 60-foot by 8-inch diameter driven tube, a fast acting centerbody valve assembly, multiple nozzles to achieve desired test conditions from Mach 6 to 18, and a test section capable of accommodating models up to 3 feet in diameter and 12 feet long. A new nozzle upgrade will soon take this capability up to Mach 22. The LENS II facility is similar in construction, incorporating 24-inch driver and driven tubes that are 60- and 100-feet in length respectively and is currently capable of running between Mach 3 and 7. Upgrades are underway to increase the performance to Mach 10. The LENS II facility is capable of test times between 100 and 20 msec at velocities from 3,000 to 8,000 ft/sec respectively. The LENS X facility is a large expansion tunnel which is assembled with major components from the LENS II facility together with new diaphragm stations and tube components.

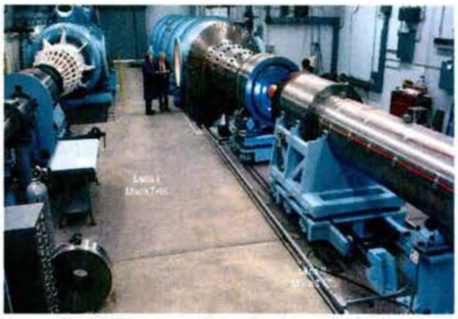

Figure 2. Photograph of the LENS I and LENS II Facilities at the Aerothermal Aero-Optics Evaluation Center

The high-pressure driver section of LENS I has the capacity to operate at 30,000 lb_f/in^2 using heated driver gases of hydrogen, helium, nitrogen or any combination of the three. The driver gases can be heated up to 750°F and the amount of each gas varied to achieve tailored interface operations for maximum test times. The driven tubes of either facility can use air, nitrogen, carbon dioxide, helium, hydrogen or any other gases or combinations of gases for model testing.

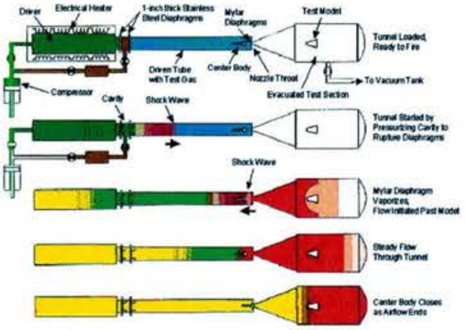

Figure 3. Basic Operation of LENS Facilities

A schematic diagram illustrating the basic operation of the shock tunnel is shown in Figure 3. Both LENS I and LENS II tunnels operate with tailored interface conditions to maximize test condition uniformity and run time. Tailored conditions are achieved by carefully controlling the pressures and gas mixtures used in the driver and driven tubes of the tunnel to achieve a condition where the contact surface between driver and driven gases is transparent to the reflected shock. Flow is initiated through the tunnel by rapidly pressurizing the center section of the double diaphragm unit causing the diaphragms to rupture. The sudden release of the driver gas generates a strong shock which travels down the driven tube, is reflected from the end wall, and travels back up the driven tube, creating a stagnant, high-pressure, high-temperature reservoir of test gas. When the reflected shock strikes the interface in its return path, the condition in the driver and driven tubes are controlled such that the contact surface is brought to rest. The reservoir of hot stationary test gas between the end wall and the contact surface is exhausted through the throat section of the nozzle into the test section in a manner similar to any blowdown tunnel. The flow through the nozzle is terminated when a fast-acting valve closes the throat section.

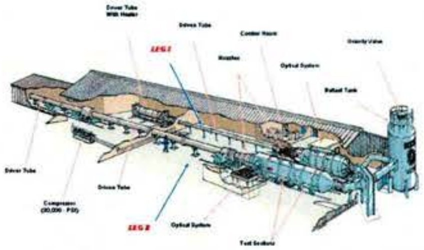

Figure 1. Schematic Drawing of the LENS I and LENS II Hypersonic Shock Tunnel Facilities and LENS X Expansion Tunnel

A velocity/altitude map for the LENS facilities is shown in Figure 4. This map includes the ascent and descent trajectories of the Australian Terrier-Orion launch vehicle that will serve as the booster for HIFiRE FRESH FX-1. The stars represent the test points of interest in this study duplicating the freestream conditions the vehicle will experience in flight. By operating the LENS tunnel under cold conditions (just above the liquefaction temperature of the airflow in the test section), large Reynolds numbers and test times can be obtained in the LENS I facility for studies where only Mach number, Reynolds number simulation is required. A Reynolds number and Mach number performance plot for the LENS facility, again including the FRESH FX-1 trajectory, is shown in Figure 5. A complete listing of LENS facility capabilities is shown in table form in Figure 6 and can be found in the references [AAEC Staff 2004].

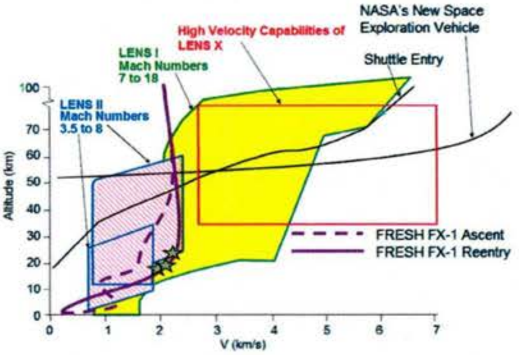

Figure 4. LENS Facility Altitude Velocity Map

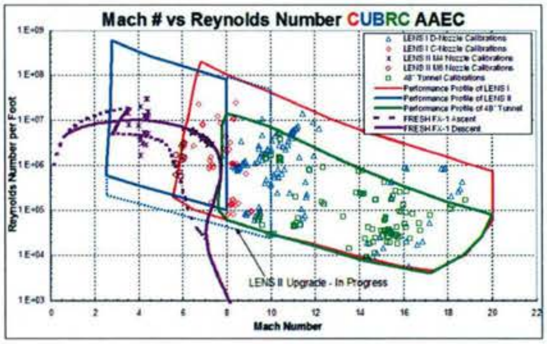

Figure 5. Mach Number/Reynolds Number Envelope

LENS I
Velocity Range (ft/sec)
3,000 – 15,000
Altitude (kft)
25 - 300
Mach Numbers
8.0 - 18.0
Reynolds Numbers (1/ft)
1.0E4 - 1.0E8
Test Time (ms)
up to 25
Nozzles
Mach 8 – 10 (48" Exit)
Mach 10 – 18 (48" Exit)

LENS II
Velocity Range (ft/sec)
2,500 – 9,000
Altitude (kft)
SL - 200
Mach Numbers
3.0 - 10.0
Reynolds Numbers (1/ft)
1.0E5 - 1.0E9
Test Time (ms)
up to 100
Nozzles
Mach 3 – 5 (42" Exit)
Mach 5 – 8 (60" Exit)

LENS X
Velocity Range (ft/sec)
14,000 – 22,000
Altitude (kft)
120 - 250
Mach Numbers
14.0 - 22.0
Reynolds Numbers (1/ft)
1.0E3 - 1.0E6
Test Time (ms)
up to 4
Nozzles
Mach 14 – 22 (60" Exit)

Figure 6 Operational Range of LENS Facilities

B. Heat Transfer Instrumentation

For these studies we primarily employed platinum thin-film heat transfer instrumentation similar to those designed at Cornell Aeronautical Laboratory (CAL) in the late 1950s and refined over the past 50 years. The platinum thin-film heat transfer instrumentation employed in these studies have proven to be the most accurate measurement technique in supersonic and hypersonic test facilities, and the small size of the sensing element coupled with the insulating substrate make them ideal for measuring high resolution heating levels and spacing of the heating on the surface of the model. CUBRC has calculated the accuracy of the heat transfer measurement to be ±5%.

The thin-film heat transfer gauge is a resistance thermometer that measures the local surface temperature of the model. The theory of heat conduction is used to relate the surface temperature history to the rate of heat transfer. Since the platinum resistance element has negligible heat capacity, and hence negligible effect on the Pyrex surface temperature, the gauge can be characterized as being homogeneous and isotropic with properties corresponding to those of the Pyrex. Furthermore, because of the short duration of shock tunnel tests, the Pyrex can be treated as a semi-infinite body. Examples of the types of thin-film instrumentation employed in this test can be seen in Figures 7-8. Because of the requirement to obtain transitional data in this program all the thin-film sensors needed to be specially matched and contoured to the surface of the model. Using very small sensors (Figure 7b) on the cone section (Figure 8) greatly helped to achieve an acceptably smooth model. There is the potential to obtain erroneous transition data from any misaligned sensors tripping or disturbing the flow.

Figure 7a. 0.125" Thin-film Heat Transfer Instrument

Figure 7b. 0.040" Thin-film Heat Transfer Instrument

The platinum thin-film sensor, with a frequency response of over 500 kHz, is also ideal in obtaining fluctuating heat transfer levels. This information is important to define the transitional flow characteristics on the model. If an adequate amount of sensors are placed in the transition zone the transition process can be accurately followed from the initial disturbances, to the turbulent bursts, to the fully turbulent levels. Typically transition is viewed as occurring at a particular geometric point, but in real life the transition front can be described as moving forward and backward over time or as a series of bursts that break out and move downstream. The thin-film sensor is the most accurate method to describe the limits of the movement and the associated heating rates.

During the first phase of the experimental program the model contained over 50 platinum thin-film sensors, distributed along the length of the model and at 0, 90, 180, and 270 degrees around the model. This number was doubled between entries to over 100 sensors of which 30 were placed in the cone/flare region to accurately measure the separation/reattachment flow.

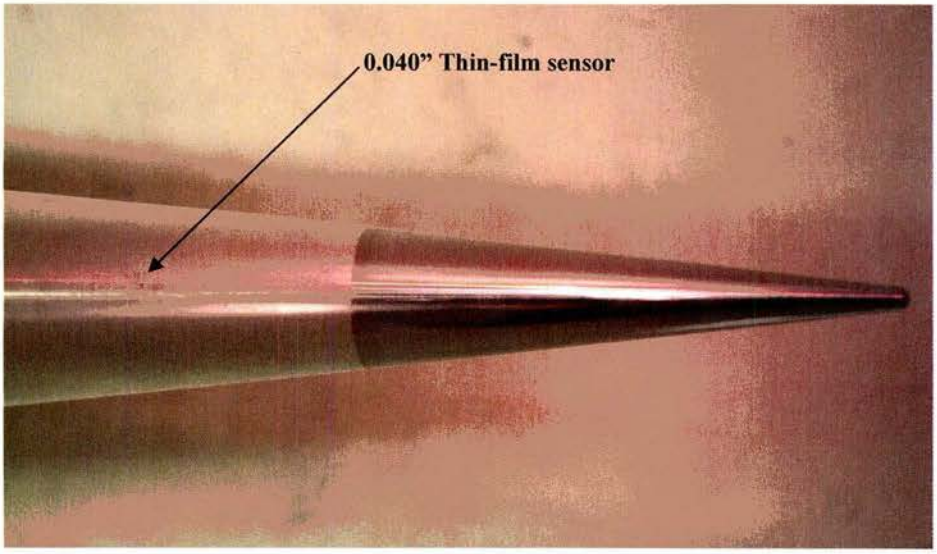

Figure 8. 0.04" Thin-film Sensors Placed in FRESH FX-1 Nose Cone

C. Pressure Instrumentation

For these studies, we primarily employed piezoelectric pressure gauge instrumentation that, like the platinum thin-film sensor, was originally designed at Cornell Aeronautical Laboratory. These gauges employ a diaphragm design and read the model pressure versus a pretest baseline pressure (differential pressure). In the data reduction process this baseline, or pre-run pressure, is subtracted off the final measurement to yield an absolute measurement. Additionally, these transducers are mounted close to the surface of the test article so that orifice effects and fill times are negligible. The piezoelectric pressure transducers, manufactured by PCB, are capable of accurately measuring pressures within ±3%. Figure 9 shows a typical PCB piezoelectric pressure transducer.

Where size constraints do not allow for PCB style instrumentation CUBRC employs both Endevco and Kulite piezoresistive type transducers. These transducers have a very small sensing footprint and can be installed in difficult geometry locations. These sensors also typically have a higher frequency response (~100 kHz) than the standard piezoelectric sensors we employ. The piezoresistive strain gauge-type transducer also has an accuracy of ±3%. Figure 10 shows a typical Kulite style transducer.

Pressure gauges employed by CUBRC are calibrated installed in the test article whenever possible. Calibration is carried out by subjecting each gauge to a traceable, steady pressure pulse lasting tens of milliseconds to duplicate what the gauge will experience during testing. This will occur over the range of expected pressures that the gauges will experience during testing.

Unique for this test is the use of a PCB time of arrival pressure sensor for measurement of 2nd mode transition frequencies. These sensors are of the type PCB 132A32 and are coupled with PCB 482A22 type signal conditioners. This combination has been reported in other studies to have successfully measured 2nd mode frequencies but the goal of this program is to attempt to measure these frequencies at flight duplicated altitude and velocity conditions [Estorf 2008].

Figure 9. Typical PCB Piezoelectric Pressure Transducer

Figure 10. Typical Kulite Piezoresistive Transducer

III. Model Design and Construction

The basic geometry for the HIFiRE FRESH FX-1 flight vehicle was given to CUBRC by AFRL and is shown in Figure 11 [Kimmel 2007]. The geometry consists of a blunt nose, 7° cone, flat cylinder section, a short 33° flare section and another flat cylinder aft end which ties into the booster. The CUBRC model represents a full-scale match of this configuration minus the slot that can be seen in the flare section. This slot will be present in the flight geometry to perform inlet mass capture optical measurements as they might relate to scramjet design. At this time it was deemed unnecessary to include this portion of the program in the CUBRC ground test. All model hardware components were machined on site at CUBRC and the as-built model is shown in Figure 12. This original configuration had a removable sharp nose and 37° degree flare section, both of which can be easily changed while the model is in the tunnel. Additional blunt noses of radius 2.5 and 5.0 millimeters were also manufactured. All the noses had considerations made for the inclusion of an electrical resistance cartridge heater that would be used to heat the nose to predicted flight temperatures so that wall temperature effects could be studied. The

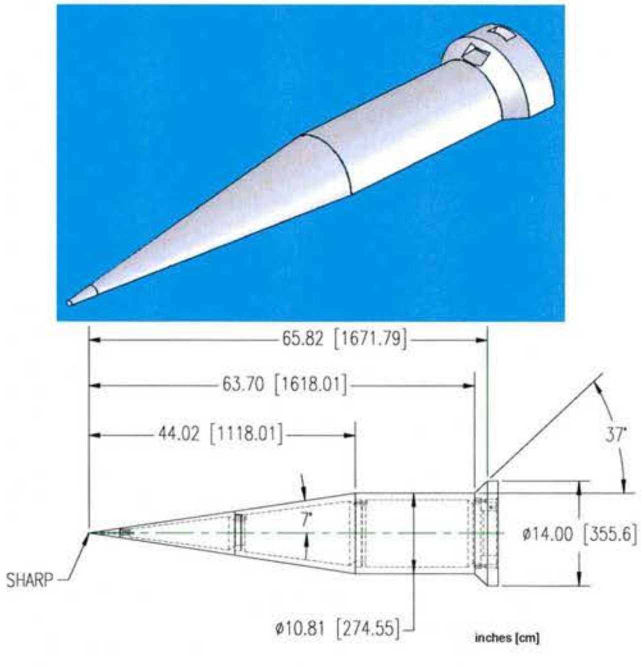

Figure 11. Basic FRESH FX-1 Flight Geometry

temperature was monitored with several thermocouples embedded in the nose material and additionally the thin-film instrumentation installed in the cone was employed to specify the temperature profile down the length of the cone. CUBRC also constructed additional flare angles of 27°, 30°, and 33°. While the 37° flare angle was supported by preliminary numerical predictions, our correlations based on our earlier studies in shock wave/turbulent boundary layer interaction [Holden 1972, Holden 1970, Holden 1986] suggested that this angle was too large and that flare angles between 30° and 33° would achieve the required well-defined turbulent interaction region at the cylinder/flare junction. To assess the flare angle effectiveness during the first phase of the program we employed high speed Schlieren video coupled with the results from earlier related studies to suggest the flare angle that should be employed on the flight vehicle. An installation diagram and photograph of the model installed in the LENS I facility is shown in Figure 13. After the conclusion of the first phase data analysis concluded that the optimal flight configuration should consist of the 2.5 mm nose tip and the 33° flare to achieve the goals of the flight test. This configuration would be employed almost exclusively in the second phase of the ground test. The first phase results were also used to identify placement additional heat-flux sensors including the transition region on the cone and a large amount of instrumentation in the cylinder/flare junction region to accurately measure the heat flux due to separation and shock interaction. A photograph of the cylinder/flare region can be seen in Figure 14 and the new overall instrumentation layout including the extended length flare is in Figure 15.

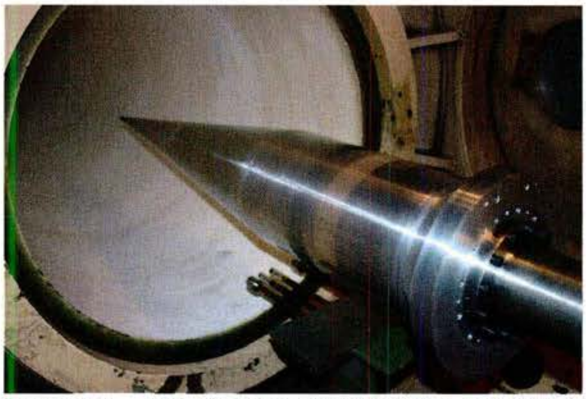

Figure 12. The As-Built FRESH FX-1 Installed in LENS I

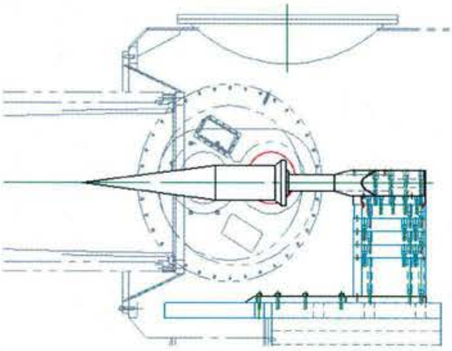

Figure 13. Drawing of Installed FRESH FX-1 Model in LENS I

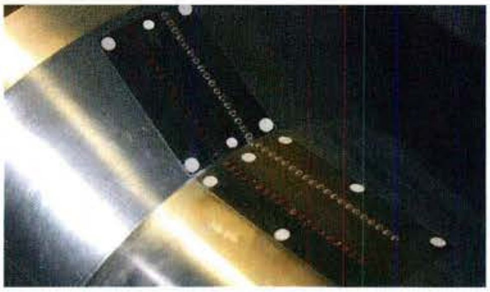

Figure 14. Second Phase High Fidelity Flare Instrumentation

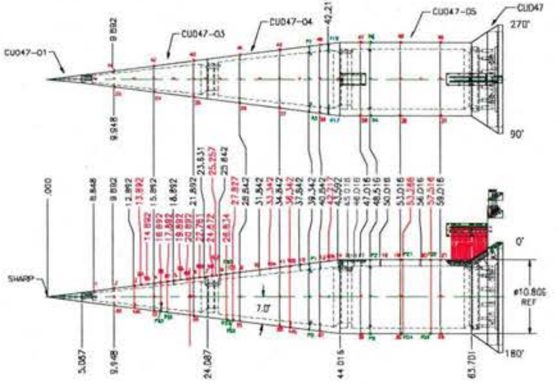

Figure 15. HIFiRE Phase II Instrumentation Layout

IV. Selection of Freestream Conditions and Facility Flow Calibrations

The FRESH FX-1 flight trajectory as specified to CUBRC by AFRL is shown in Figures 16 and 17. [Kimmel 2007] Data will be taken over the entire flight from launch until such time as the vehicle or sensors fail during descent. The points where ideal transition conditions exist are marked with stars. The filled in stars additionally correspond conditions that are new to the second entry and are primarily specified to assess trip effectiveness. How these points fall into LENS capabilities were shown in Figures 4 and 5. Each of the unique test conditions, shown in Table 1, that are to be run during the experimental program are first calibrated with test runs in the facility after being predicted computationally. The computational work allows for having to make fewer calibration runs at each condition and more importantly it adds greatly to the understanding of what is happening in the freestream at every condition. This will be important later when full model computations are performed. Basic instrumentation associated with the experimental calibration of the LENS facilities include: pressure sensors to monitor the initial driver and driven gas pressures and temperatures, thin-film resistance and piezoelectric pressure gauges installed at fixed locations on the driven tube to monitor the speed of the incident shock wave as it propagates down the tube, pressure sensors in the endwall region to measure the reflected shock reservoir pressure, a pressure sensor in the initially evacuated test section, and a survey rake installed in the test section to measure pitot pressure, static pressure and stagnation point heat transfer in the freestream. From these measurements and rake assembly, a comprehensive data set for each test condition was taken to calculate freestream conditions, core size, and flow uniformity of the freestream flow. A typical survey rake assembly is shown in Figure 18 together with the flowfield survey probes at the exit plane of the nozzle.

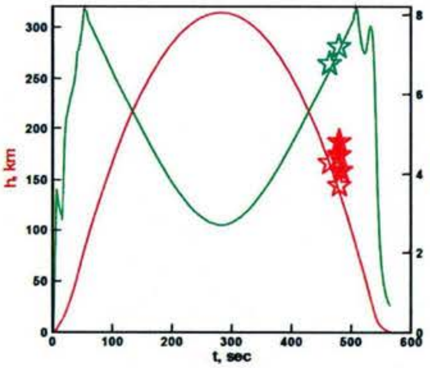

Figure 16. Overall Flight Trajectory of FRESH FX-1

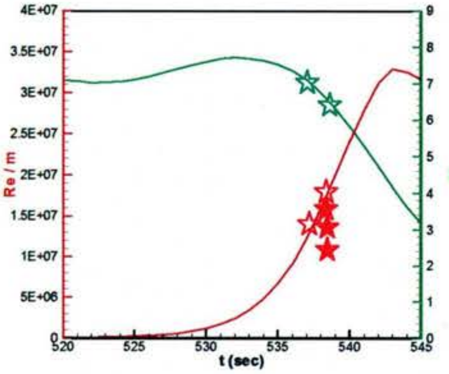

Figure 17. Detail Mach Number Reynolds Number Trajectory Plot Showing Area of Interest for Transition Experiments

High-frequency pressure instrumentation is typically used in the pitot probes. However, in regions where flows generate high thermal loads, we must employ thermal protection systems that lower the frequency response. Total temperature measurements are made in the lower enthalpy flows with shielded thermocouple probes while total heat transfer measurements are made with miniature thin-film or coaxial instrumentation placed in the stagnation region of a hemispherical nosetips.

The first step in determining the test conditions in the LENS facility is to determine the conditions observed in the reservoir. This is accomplished via a combination of measurement and theory. The initial and final (reservoir) pressures are measured by a group of redundant pressure gauges in the endwall of the driven tube. The shock speed is also measured by a series of fast-response gauges down the length of the driven tube which react as the incident shock moves through the test gas. Using these pieces of information, the unique reservoir conditions may be computed from generalized equilibrium conditions and wave propagation theory after both the incident and

Condition	Velocity (ft/sec)	Altitude (kft)	Temperature (°R)	Pressure (psia)	Density (slugs/ft^3)	Mach Number (-)	Reynolds Number (1/ft)
A	6,320	58.5	386	1.12	2.4E-4	6.58	5.3E+6
B	7,160	69.1	417	0.67	1.4E-04	7.16	3.1E+6
C	7,160	78.2	417	0.44	0.9E-04	7.16	2.0E+6
D	7,160	88.3	417	0.22	0.5E-04	7.16	1.0E+6
E	7,160	101.8	417	0.11	0.2E-04	7.16	0.5E+6

Table 1. Nominal Flight Conditions Duplicating Those Predicted from the Flight Trajectory

the reflected shocks have passed through the test gas. The computation of the reservoir assumes full thermodynamic and chemical equilibrium at all points. This is a safe assumption, as the pressures and temperatures after the shocks are very large, thus making relaxation times exceptionally short. Relevant translational, rotational, and vibrational modes are considered in the energy of the molecules.

These results are now compared with the pre-calibration computational results. Figure 19 shows an example of the comparison of the Navier-Stokes and the measured pitot profile measurements for Mach 6.5, demonstrating the level of agreement obtained between CFD and experiment in the LENS programs. Pitot pressure is used as a measure of freestream accuracy for two primary reasons: (1) it is a directly measurable quantity, and (2) it is sensitive to the momentum in the flowfield. Hence, it is a good choice to judge the accuracy of the freestream specification. This is the same process CUBRC employs to prepare for any experimental program in the LENS facility.

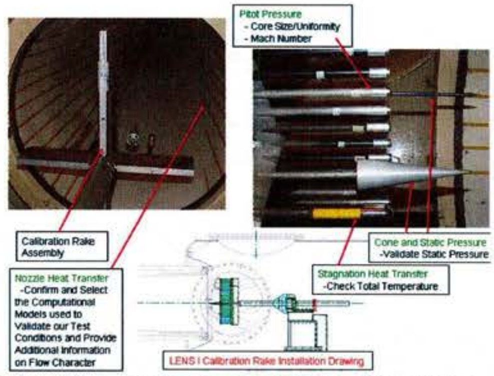

Figure 18. Photograph of Calibration Rake Mounted Inside Test Section of the LENS I

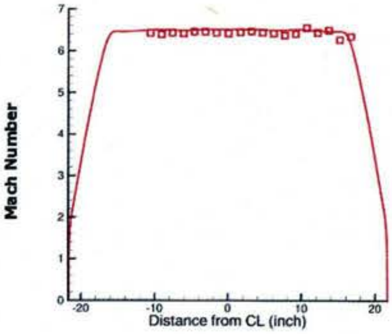

Figure 19. Comparison between Experimental and Computational Nozzle Profile

IV. Review of Experimental Results from Phase I

The first part of the ground test program [Wadhams 2007] concentrated on specifying the nosetip bluntness that provides well-defined laminar, transitional, and turbulent regions on the cone section for each freestream condition including several angle of attack variations. Initial tests employing the sharp nosetip are shown for all heat transfer rays (0°, 90°, 180°, and 270°) in Figure 20. Here for Mach Number of 6.5 and Reynolds Number of 5.0 million per foot the turbulent region extends forward onto the removable nose section of the cone where no sensors exist. To confirm this assertion of turbulent flow the semi-empirical turbulent flow prediction method of Van Driest [Van Driest 1951] is employed and shows good agreement when compared with the experimental results for the length of the cone. The semi-empirical laminar prediction method of Cheng [Cheng 1961] is also shown with the experimental data always remaining well above this level by a factor of greater than 4. Computational results employing the DPLR code were done in parallel with the experimental program and will be discussed in Section V. Pressure results were also checked with simple Newtonian calculations and again show good agreement with the experimental results and confirm the specified freestream conditions.

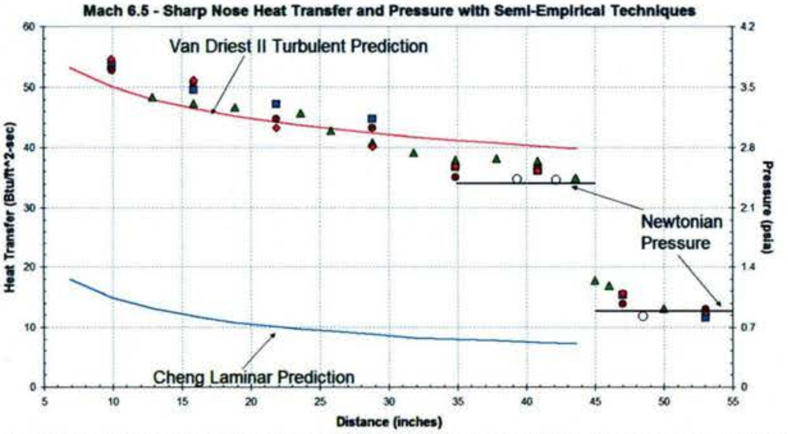

Figure 20. Mach 6.5 and Reynolds Number 5.0E6 per Foot Heat Transfer and Pressure Measurements with Sharp Nose Configuration Showing Transition Forward of First Sensor

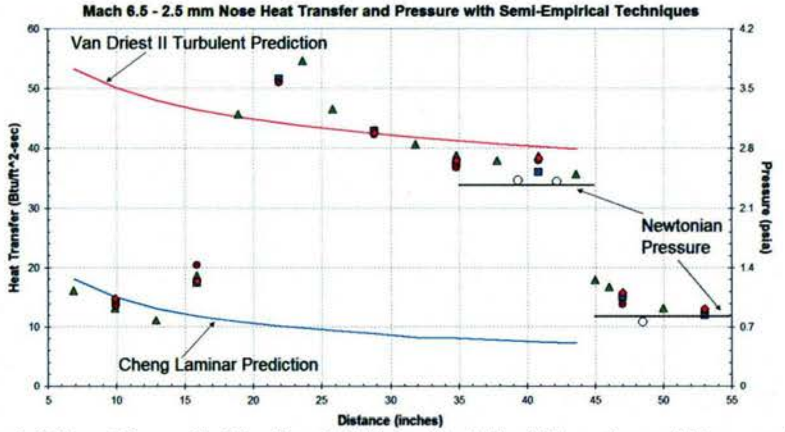

Figure 21. Mach 6.5 and Reynolds Number 5.0E6 per Foot Heat Transfer and Pressure Measurements with 2.5 mm Nose Configuration Showing Transition Delayed to 15 inches

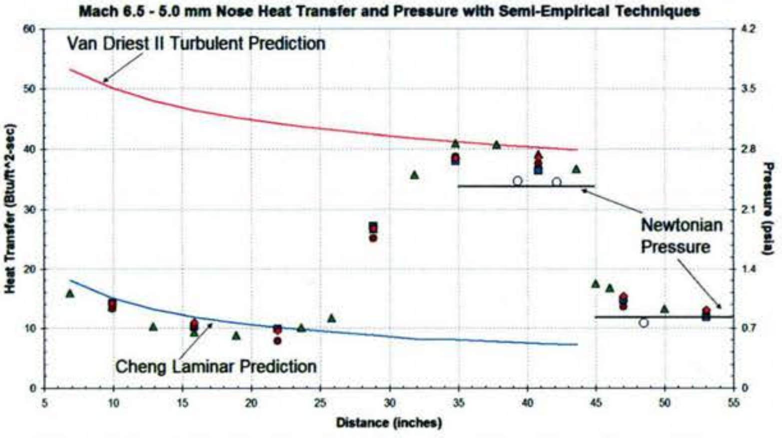

Figure 22. Mach 6.5 and Reynolds Number 5.0E6 per Foot Heat Transfer and Pressure Measurements with 5.0 mm Nose Configuration Showing Transition Delayed to 25 inches

The next experiment was conducted at the same freestream condition but the sharp nose was replaced by a blunt nose configuration of 2.5 millimeter radius. The heat transfer and pressure results are shown in Figure 21. The addition of the bluntness effects results in delaying the transition point to almost 15 inches. A well-defined laminar region now exists and agrees well with the Cheng prediction. There is a well-defined turbulent region that extends for 15 inches before the flow turns onto the cylinder section that agrees well with the Van Driest prediction. Also as with the sharp case there is good agreement between the pressure levels and the Newtonian prediction.

One additional bluntness, 5.0 millimeters, was also tested, the results of which are shown in Figure 22. Here while the laminar region is very well defined the fully turbulent region has been further delayed with increased bluntness and now occurs at 25 inches in front of the cone/cylinder junction.

The bluntness tests were then repeated for freestream Mach Number of 7.2 and Reynolds Number of 3.0 million per foot to allow a decision on which bluntness produced the best defined flow characteristics on the nose. The sharp nose case was omitted at this condition due to the low level of confidence that a well-defined environment would be obtained based on the result from the earlier studies. Figure 23 shows the Mach 7.2 results for the 2.5 millimeter bluntness condition. Comparing this result to the one at Mach 6.5 we see that the transition point has moved downstream 3 inches. This result is encouraging in that the transition point does not move much due to the combination of Mach Number and Reynolds Number changes between the two conditions.

The 5.0 millimeter bluntness was also tested and the resulting data can be seen in Figure 24. The additional bluntness here moves the transition point another 2 inches downstream comparable to the results for the Mach 6.5 condition. Again, the transition location is similar to the results for the same bluntness at Mach 6.5.

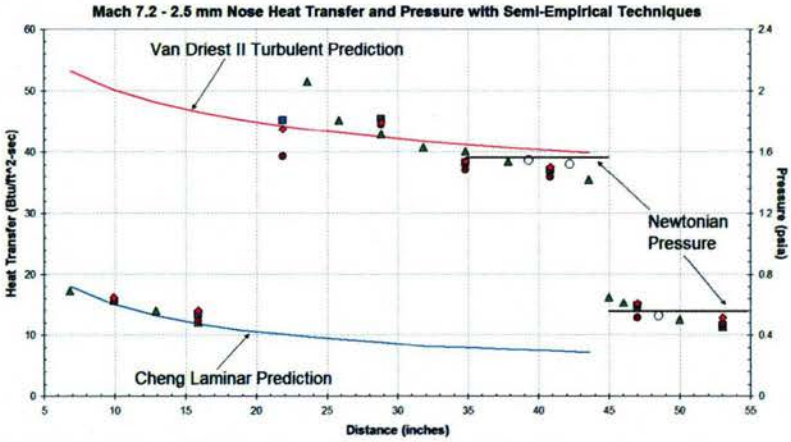

Figure 23. **Mach 7.2 and Reynolds Number 3.0E6 per Foot Heat Transfer and Pressure Measurements with 2.5 mm Nose Configuration Showing Transition Delayed to 18 inches**

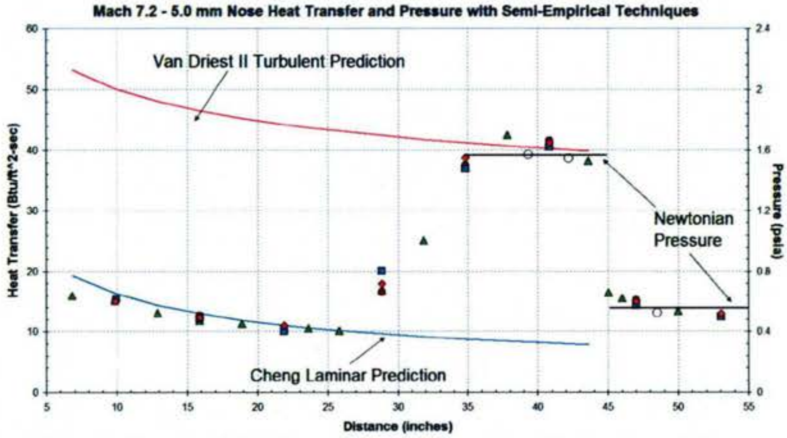

Figure 24. **Mach 7.2 and Reynolds Number 3.0E6 per Foot Heat Transfer and Pressure Measurements with 5.0 mm Nose Configuration Showing Transition Delayed to 27 inches**

These results at Mach 7.2 along with those at Mach 6.5 definitively show that the most well-defined flow configuration is produced with the 2.5 millimeter nose bluntness. While there are definable flow regions employing the 5.0 millimeter bluntness the turbulent region is too close to the cone/cylinder junction point considering there is the possibility that the transition point in flight could be further downstream. This consideration will elaborated on in the stability analysis discussion in Section V. Thus for zero degrees angle of attack the 2.5 millimeter bluntness case provides well-defined transition phenomena over the cone with a fully turbulent boundary layer ahead of the flare at the three conditions specified on the predicted flight trajectory. In the next set of studies the angle of attack effects will be explored to see if the choice of nose bluntness is significantly affected.

Also in this phase of experiments, heat transfer and pressure measurements were obtained for angles of attack of 1° and 5°. The flight program is designed to stay within angles of attack of 1° and 2°, but for the ground test the extreme angle of 5° was selected. These experiments were performed exclusively with the 2.5 millimeter radius nose to further validate the decision to employ this bluntness in flight. The heat transfer measurements for the two attitudes tested on the windward side of the model, shown in Figure 25, demonstrate that transition moves forward with increasing angle of attack until, at a model attitude of 5°, transition begins close to the nosetip and it is completed at the 15 inch axial station. These measurements were later repeated in the ground test program at both 1° and 5° angle of attack during the flare angle portion of the study and are also shown in Figure 24 and show excellent repeatability.

Similar leeside measurements are shown in Figure 26. Transition characteristics vary only a little between model attitudes of 0° and 1° and show similar transition locations. However, at 5° incidence, the transition point has moved well forward on the cone resulting in turbulent heating over 35 inches of the cone. Additional leeside measurements were again made during the flare angle studies and similarly show excellent repeatability. This repeatability has been calculated to be within 5%.

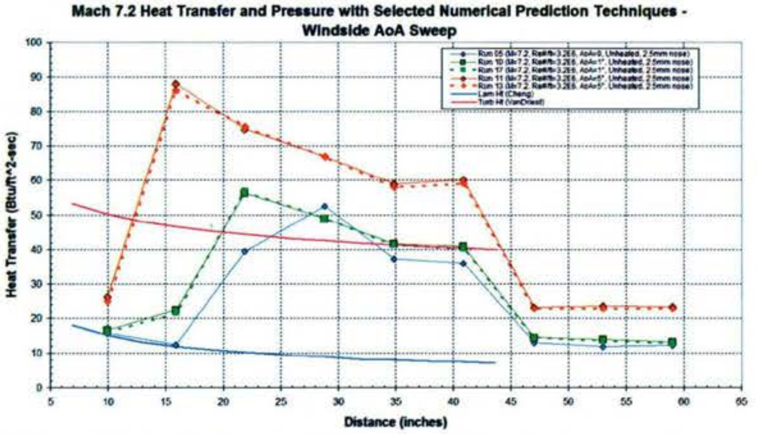

Figure 25. **Mach 7.2 and Reynolds Number 3.0E6 per Foot Heat Transfer and Pressure Measurements with 2.5 mm Nose Showing Windward Angle of Attack Effects on Transition**

These results show that for the Mach Number, Reynolds Number, and angle of attack variations considered in this study the 2.5 millimeter nose bluntness is the best choice to achieve the goal of well-defined laminar, transitional, and turbulent regions during flight for code and ground test comparison and validation.

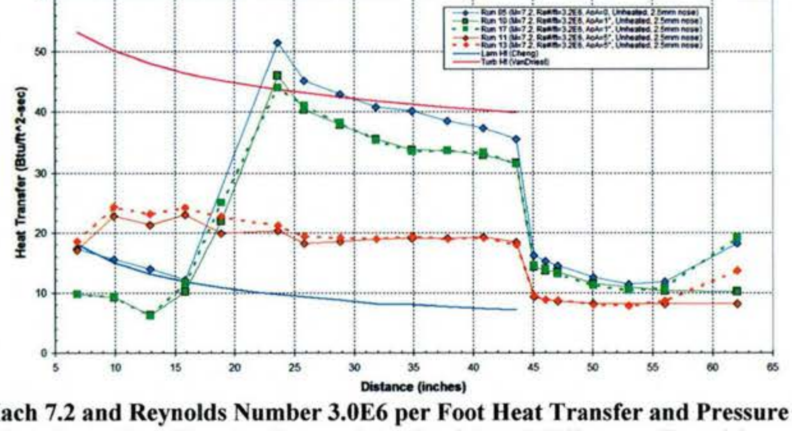

Figure 26. **Mach 7.2 and Reynolds Number 3.0E6 per Foot Heat Transfer and Pressure Measurements with 2.5 mm Nose Showing Leeward Angle of Attack Effects on Transition**

As equally important at the transition study the first phase of the ground was also designed to select the proper flare angle for the flight test. As with the transition part of the flight experiment it is important to obtain flight data in a well-defined shock wave/boundary layer interaction region so that good comparisons with ground test and computational results may be made. This requires a fully turbulent boundary layer on the cylinder surface, definable separation and reattachment regions over the cylinder flare junction, and a measurable reattached flow region over the latter part of the flare to serve as a definable boundary condition for comparison purposes. Initially a flare angle of 37° was planned for the flight vehicle, but the flow characteristics needed to be experimentally tested to confirm this choice. During the ground test the flare was to remain uninstrumented so that changes could be quickly made while the model remained in the tunnel and this confirmation was to be carried out by CUBRC's high speed Schlieren video system. This system employs a copper vapor laser and a 10,000 frame per second Phantom version 7.0 camera that is synchronized to the laser pulses and is able to essentially "freeze" the flow phenomena.

Initial tests at Mach Number of 7.2 and Reynolds Number of 3.0E6 per foot were performed with the 37° geometry. Results of these tests and a configuration diagram can be seen in Figure 27. The Schlieren photograph indicates that reattachment occurs close to or at the end of the flare so that there is not a significant attached region downstream of reattachment in which measurements could be made to define the downstream boundary conditions required to accurately evaluate the performance of the turbulence models employed in the prediction.

Configuration studies at CUBRC prior to testing suggested that a 30° flare angle would be a good choice to obtain to desired flow characteristics, but due to angle of attack concerns lengthening the separated region on the leeside of the model it was decided to start with the flare angle at 27°. The Schlieren result and the configuration drawing from this test can be seen in Figure 28. In the Schlieren photo we see that the separated region is very small and the flare shock wave extends through the boundary layer almost to the cylinder/flare junction point. This flare case would not be satisfactory for the flight case.

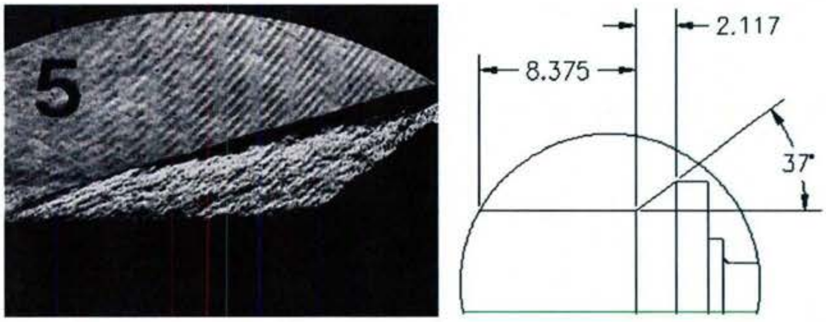

Figure 27. Schlieren Image of Flare Region at Mach 7.2 - 37° Flare Angle

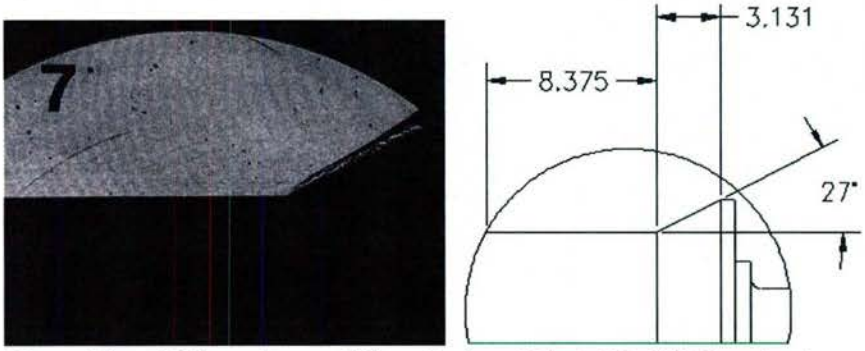

Figure 28. Schlieren Image of Flare Region at Mach 7.2 - 27° Flare Angle

The 27° degree flare was removed and replaced with a 30° flare angle and the model was retested at the same test conditions. The Schlieren image for this condition (Figure 29) now shows a slightly larger separated region and while this might be a good selection for angle of attack cases it remains too small for the required flight case geometry.

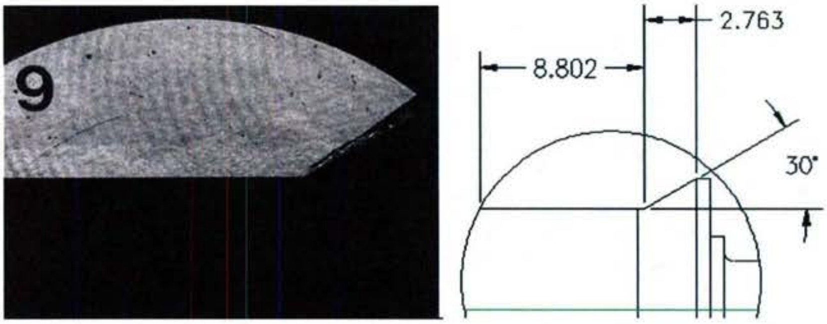

Figure 29. Schlieren Image of Flare Region at Mach 7.2 - 30° Flare Angle

The fourth and final flare angle of 33° was next tested at Mach 7.2 and produced the Schlieren image shown in Figure 30. This flare angle produced a separated region that reattached about a two-thirds of the way up the flare producing a reattachment shock. These features indicate well-defined flow characteristics that can be expected to produce data downstream of the reattachment point that can be employed as a boundary condition for computationalists to validate turbulence models. Additional tests with this flare angle are now necessary to confirm well-defined characteristics for Mach 6.5 and for the angles of attack of 1° and 5°. Figure 31 shows the results for this testing. These Schlieren shows a larger separated region when compared to Mach 7.2 in Figure 30, but the reattachment point is still on the flare with a reattachment shock and room downstream for making boundary

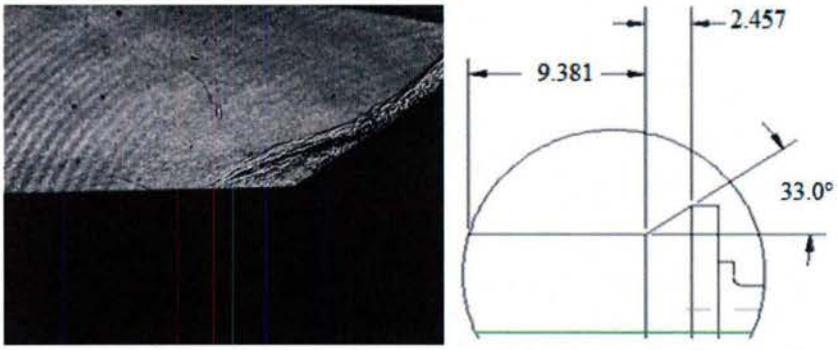

Figure 30. Schlieren Image of Flare Region at Mach 7.2 - 33° Flare Angle

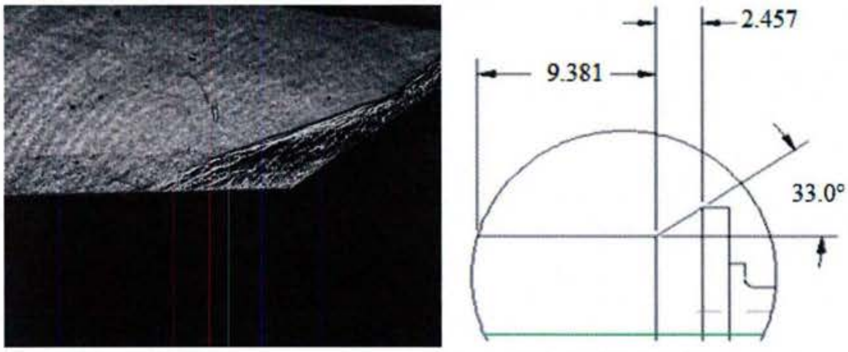

Figure 31. Schlieren Image pf Flare Region at Mach 6.5 - 33° Flare Angle

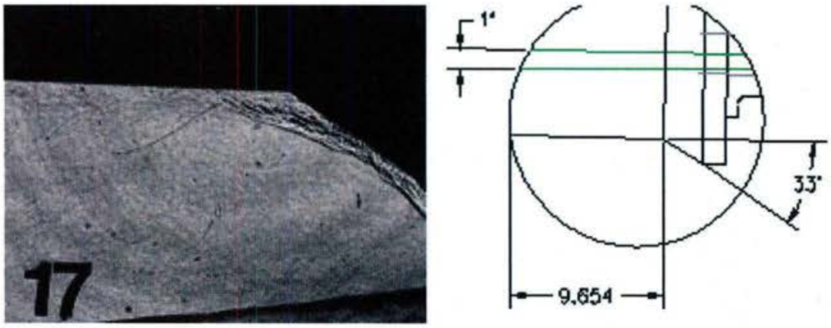

Figure 32. Schlieren Image of Flare Region at Mach 7.2 - 33° Flare Angle, 1° Angle of Attack

condition measurements. An angle of attack case is shown in Figure 32. Here we see that for the 1° case the windward flare is similarly well-defined.

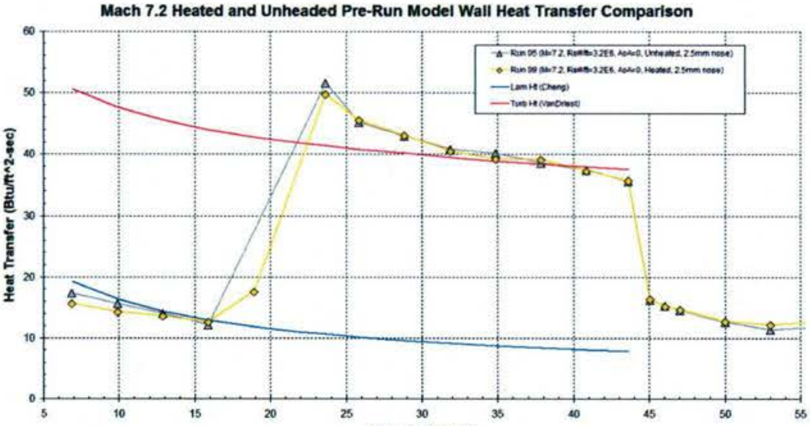

Figure 33. Comparison of Transition Location Between Unheated and Pre-run Heating of FRESH FX-1 Nose Region

A final part of the first phase involved heating the model nose to investigate the effect of wall temperature on the transition location. Employing an electrical resistance heater installed in the removable nose tip we heated the nose and cone section to 800° R. We also monitored the temperature gradient up the nose section using the installed thin-film sensors that, in their simplest form, are resistance thermometers. The actual temperature gradient is shown in Figure 33. As shown the temperature starts at 800° F at the nose and returns to room temperature by 25 inches up the nose. These temperature values were sampled immediately prior to tunnel operation. The resulting data compared to the unheated model data is presented in Figure 34. Here it is shown for the conditions and temperatures tested that there is no measurable effect of wall temperature.

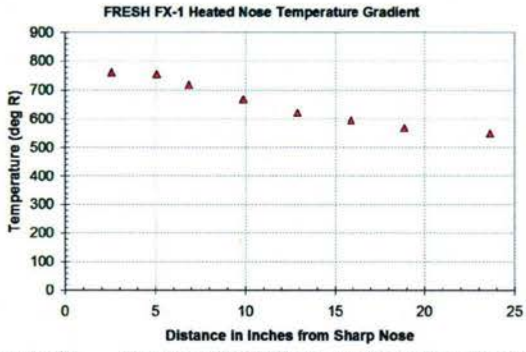

Figure 34. Pre-run Wall Temperature Gradient as Measured Thin-film Sensors

V. Experimental Results of the Current Study

A. Initial Tests and Comparison with Phase I Results

The current study began with several tests repeating model configuration and freestream conditions to confirm matching results to the first phase of testing and to obtain high-resolution transition data at these conditions for use with the STABL stability analysis code. These initial runs were also used to check out the large amount of new instrumentation in the flare region. The cone results from the second entry can be seen compared directly to the first entry results in Figures 35 and 36 for Mach 6.5 and 7.2 conditions respectively. The key data comparison in the figures is the open versus closed blue diamonds. The open diamonds represent the results from the first entry while the closed diamonds are the heat flux measurements from the second entry. Agreement between the two entries is excellent in both heat flux level and transition location. The additional heat flux sensor locations are evident throughout the transition region and add a significant amount of resolution to the region that will be very valuable in the assessment of computational turbulence modeling. Several angle of attack tests were also run at first phase conditions. These are shown in Figures 37 and 38 for the windward and leeward sides respectively and also show a high level of agreement between entries.

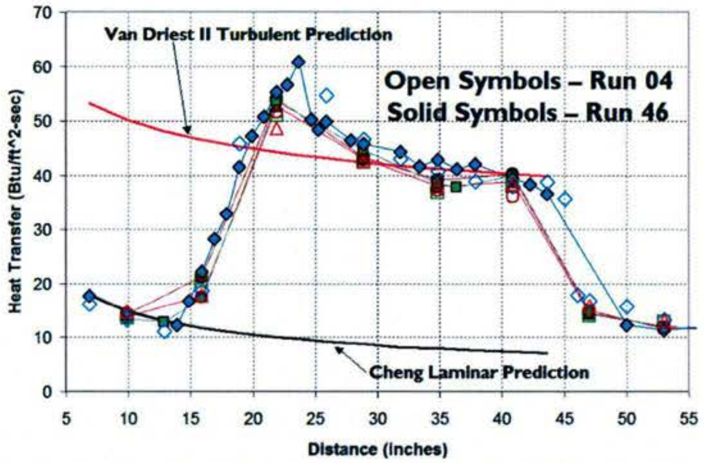

Figure 35. Comparing Mach 6.5 Transitional Heat Transfer Results from the First and Second Entries

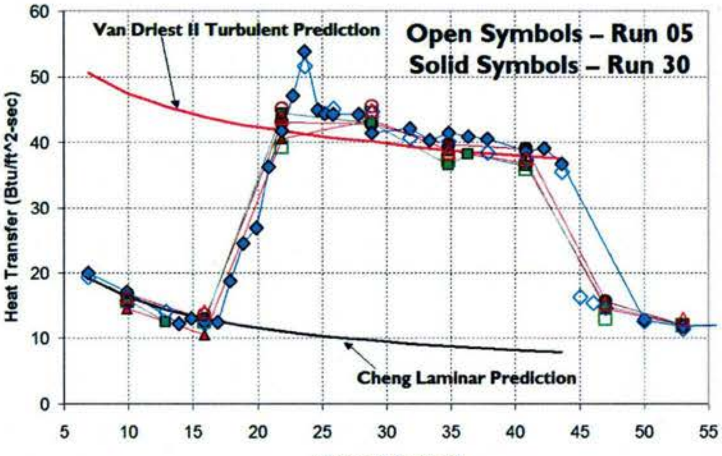

Figure 36. Comparing Mach 7.2 Transitional Heat Transfer Results from the First and Second Entries

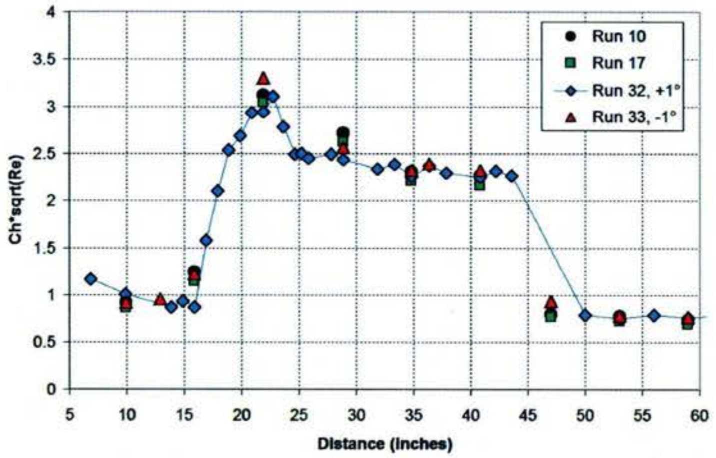

Figure 37. **Comparing Mach 7.2 Angle of Attack Heat Transfer Results from the First and Second Entries – Windward Side**

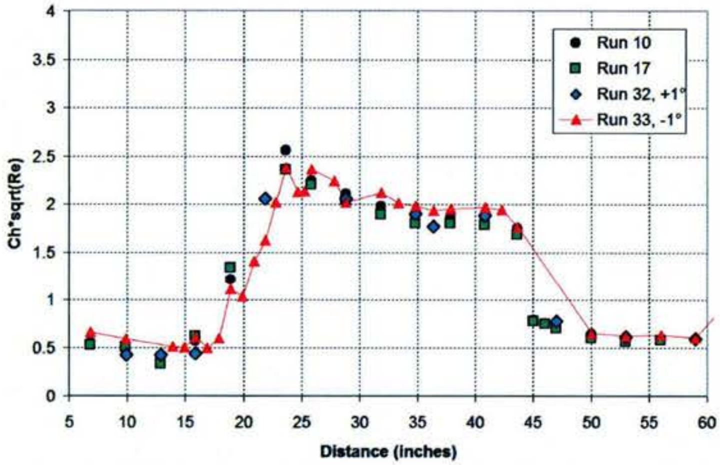

Figure 38. **Comparing Mach 7.2 Angle of Attack Heat Transfer Results from the First and Second Entries – Windward Side**

B. Studies of Trip Effectiveness

The HIFiRE flight vehicle will include a single diamond shaped discrete roughness element located 525 mm from the blunt nose tip on the surface of the cone section. This trip has been designed to extend the region in the flight trajectory where turbulent flow can be obtained over the surface of the model. To verify these design assumptions a portion of the ground test program was dedicated to testing the trip effectiveness to sustain turbulent flow onto the cylinder section through the expansion and assess the effects of the trip on the opposite side of the model and when the flow is naturally turbulent. The trip employed in the experimental program is shown in Figure 39. The trip is a diamond shape with all sides equal to 10 mm in length and a height of 2 mm. The corners have been rounded with a radius of 1/32 inches. The installed location on the wind tunnel model is shown in Figure 40. The distance here was slightly shorter than the flight location by 3 mm, but this is done intentionally to place the trip directly behind a surface heat flux sensor. The first test performed during this portion of the program

Figure 39. **Trips Employed in Roughness Studies**

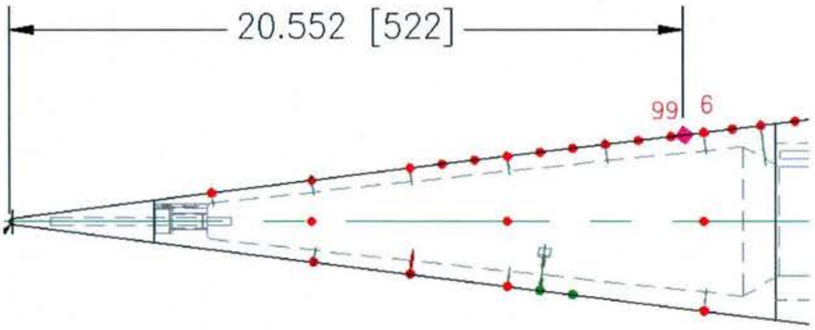

Figure 40. Trip Location as Tested

consisted of a laminar smooth body base line run. The results from this test can be seen in Figure 41 compared in nondimentional Stanton number form with a higher Reynolds test. The agreement in the laminar region is good and confirms the heat-flux measurements and freestream conditions. There may be some indication past 40 inches of the beginnings of transition, but this likely goes away as the flow expands onto the cylinder section. The trip was next applied to the surface and tests were performed over a range of Reynolds numbers and model attitudes to assess the trip effectiveness. Three zero degree angle of attack runs at Reynolds numbers from 0.5E6 to 2.0E6 are shown in Figures 42-44. In all these figures the trip location is evident due to the increase in heat flux directly in front of the trip element as the flow stagnates on the leading edge. At the higher Reynolds numbers the flow transitions close to the trip location and as Reynolds number is decrease the distance between the trip and the transition location increases. At the lowest Reynolds number the heat flux actually decreases below the laminar level due to the trip disturbance. These three runs are compared to the laminar and smooth body transitions runs in Stanton number form in Figure 45. The fifth root Reynolds number scaling in this figure allows for the correlation and collapse of the turbulent regions of the flow. There is good collapse of all the runs on the cone section once the data at each Reynolds number completes the transition process. The collapse on the cylinder section is not as good with red triangles, the lowest Reynolds number condition, falling somewhere between the fully turbulent and fully laminar levels. The uncertainty in the tripped lowest Reynolds number (0.5E6 1/ft) condition on the cylinder section results in performing the rest of the tripping studies at the next higher Reynolds number (1.0E6 1/ft) to assure a well-defined test case. Figure 46 shows the angle of attack test performed at the 1.0E6 1/ft Reynolds number condition and shows effective tripping for all tested model attitudes and assuring turbulent flow on the cone section that persists onto the cylinder section. The effect of the trip element on the opposite side of the model was also assessed at this time but these results will be discussed later with the rest of the flare data.

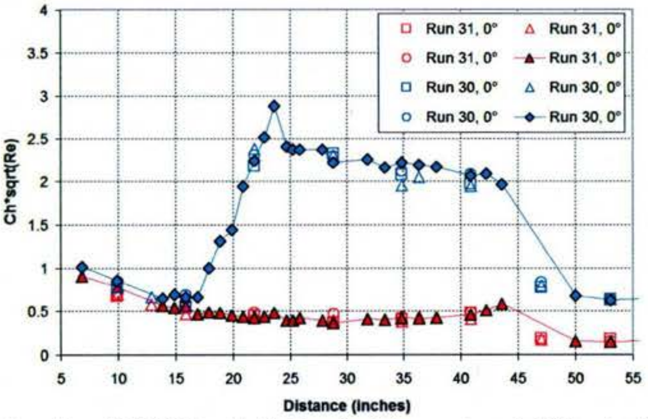

Figure 41. Laminar Baseline (0.5 Million Re#) Run for Comparison in Tripping Studies

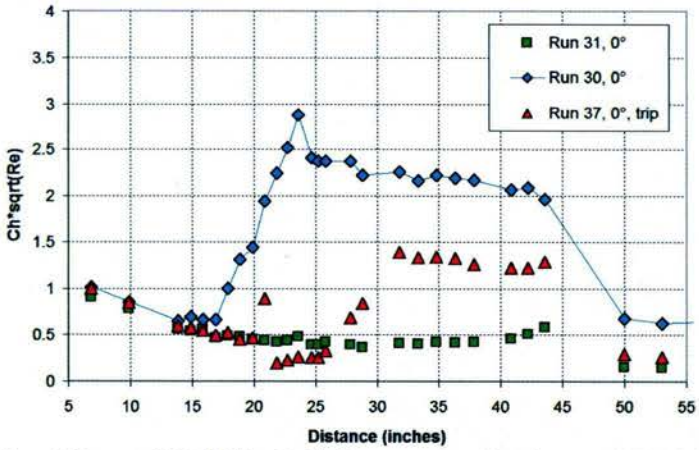

Figure 42. Tripped Run at (0.5 Million Re#) Compared to Laminar and Turbulent Conditions

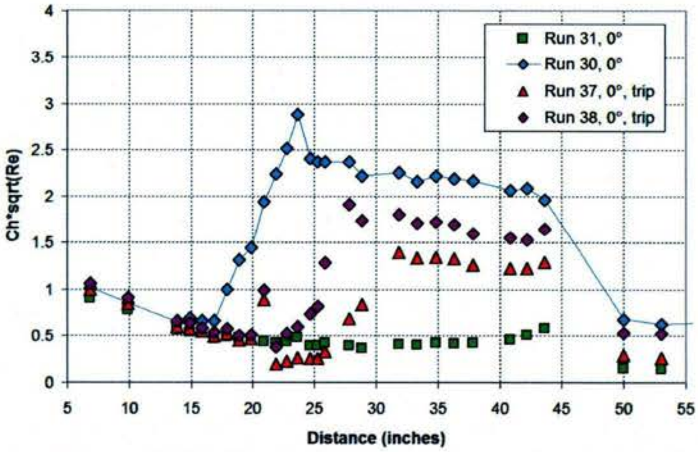

Figure 43. Tripped Run at (1.0 Million Re#) Compared to Laminar and Turbulent Conditions

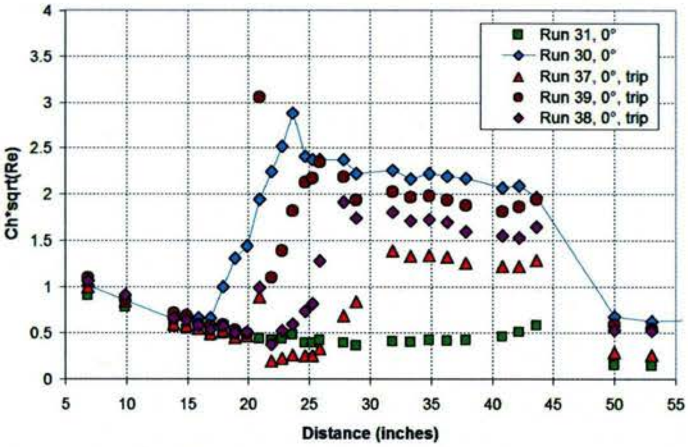

Figure 44. Tripped Run at (1.0 Million Re#) Compared to Laminar and Turbulent Conditions

Second Entry Instrumented Flare Results

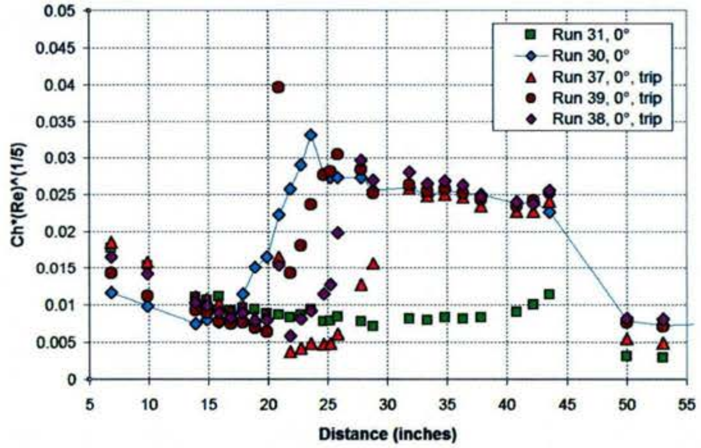

Figure 45. **Tripped Run at (1.0 Million Re#) Compared to Laminar and Turbulent Conditions**

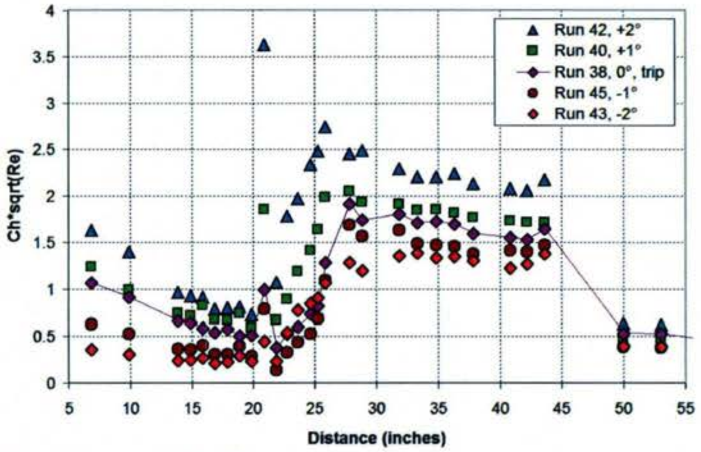

Figure 46. **Tripped Run at (1.0 Million Re#) Compared to Laminar and Turbulent Conditions**

C. Second Entry Flare Region Heat Flux Results

In Section IV the first phase flare selection process was described in detail employing high-speed schlieren movie stills. These schlieren movie stills were also employed to layout the instrumentation to measure the heat flux and pressure in this region during the second phase of the ground test. Two metal inserts were constructed and instrumented with the maximum number of instruments being limited only by the physical size constraints. Pictures and drawings of these inserts can be seen in Figures 14 and 15. Example flare data from the initial runs can be seen in Figure 47. Here we see the initial turbulent level of heat transfer (red triangle) and pressure (blue diamond) on the cylinder surface with a jump after 62 inches as the flow separates and then increases to a peak level at 65.5 inches during the reattachment and interaction process. Agreement between pressure and heat transfer looks good in both the separated region and peak interaction region. The schlieren images on the flare region between the first and second phases were also in good agreement. While all of these things were encouraging that the experiment was going to be a success the lack of a well-defined boundary condition down stream of the peak region was cause for concern. The flare length in the current configuration appeared to be too short for the reattachment and compression process to complete and the flow return to simple cone pressure levels. This boundary condition data could be the difference in the ability to properly model the turbulent flow in this region. To correct this situation the decision was made to construct an additional flare extension that could be easily added to the already existing flare length. The data from the first run after this configuration change can be seen in Figure 48. Here comparisons of the heat transfer and pressure from both runs are presented and there is good agreement between the two runs in separated region length, peak location, and overall heat flux levels, but with the additional flare length enough data now should result in a well defined experiment that also is of code validation quality.

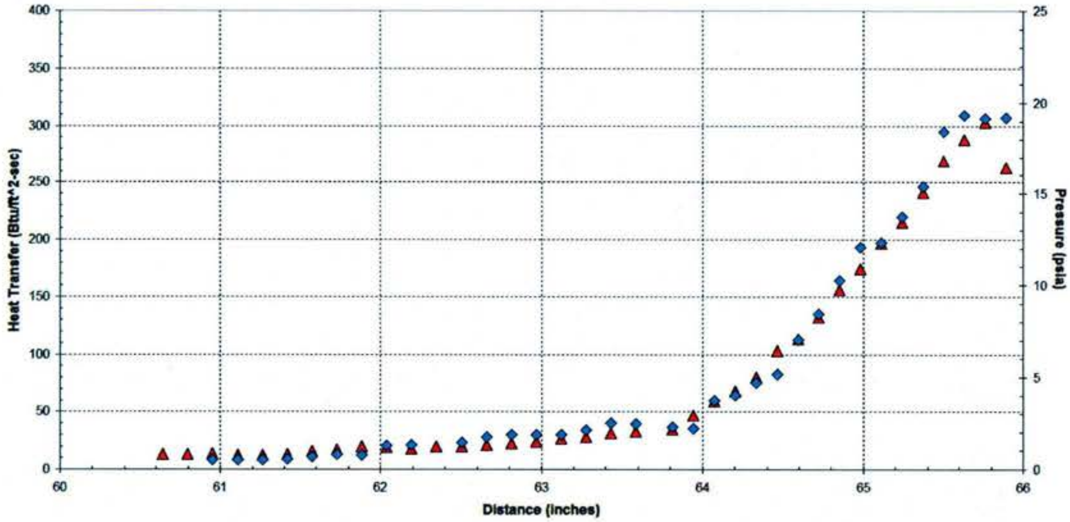

Figure 47. Initial Flare Region Results at Freestream Flight Conditions

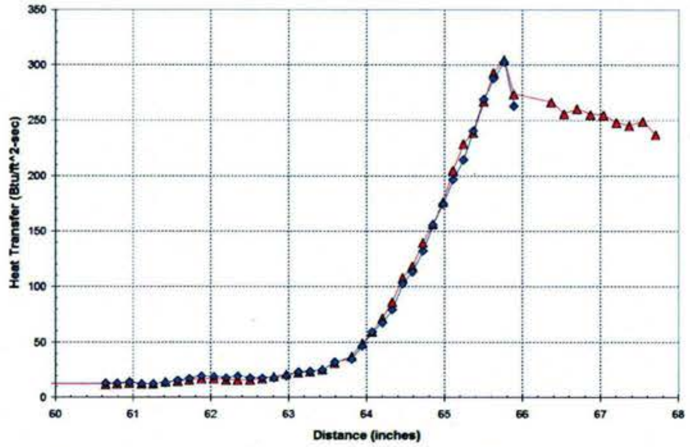

Figure 48. Heat Flux Results Comparing the Flight Length Flare and the Extended Length Flare

Upon the resolution of the flare length the ground test program proceeded as planned. Figure 49 shows results from an angle of attack sweep over anticipated flight angle of attack range. The instrumented flare sections for these studies were placed on the bottom side of the model so that the region could be filmed with our high-speed schlieren system. The results show that at positive angles of attack the angle of the cone and flare sections get larger with respect to the flow and the separated region shortens and moves the peak heating location further upstream. At negative angles of attack the cone and flare angles get smaller with respect to the flow and as expected the separation regions increase in size and move the peak heating location down stream. Similar angle of attack results with the discreet diamond roughness element were also obtained at lower than flight Reynolds numbers. These results can be seen in Figure 50. The flight test will employ these results directly to select the appropriate flight instrumentation and determine their proper locations on the flight vehicle. Because of this end result several additional ground test points were selected to better define what to expect in flight and aid in the analysis of the flight data post-flight. During flight the vehicle will be spinning and have a small coning motion that results in the angle of attack. At lower Reynolds numbers this roughness element would provide transition data on one side of the model while the other will remain laminar. This situation needed to be verified in the ground test and the first additional test point consisted of placing the discreet diamond roughness element on the opposite side of the test model from the detailed flare instrumentation to see if at angle of attack the effect of the roughness fed around the model and caused transition of the lee side of the vehicle. The results of this study, shown in Figure 51, show no effect of the roughness on the leeside of the model. The second additional point entailed removing the extended length flare, returning the model to the flight geometry, and comparing flight length flare test with the extended length flare tests. These results are shown in Figure 52, and surprisingly do not show very little difference between the two configurations. This was also explored computationally with similar results [MacLean 2008].

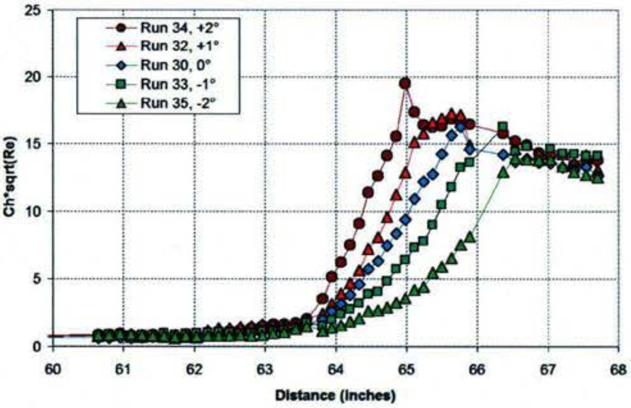

Figure 49. **Smooth Body Flare Region Heat Flux Results for Flight Angle of Attack Range**

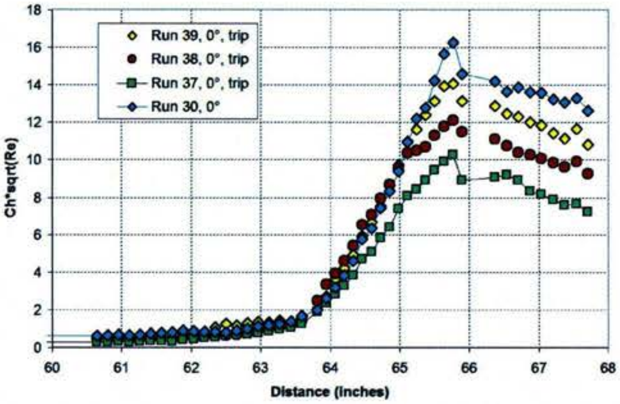

Figure 50. **Tripped Mach 7.2 Forebody Flare Region Heat Flux Results for a Range of Reynolds Numbers**

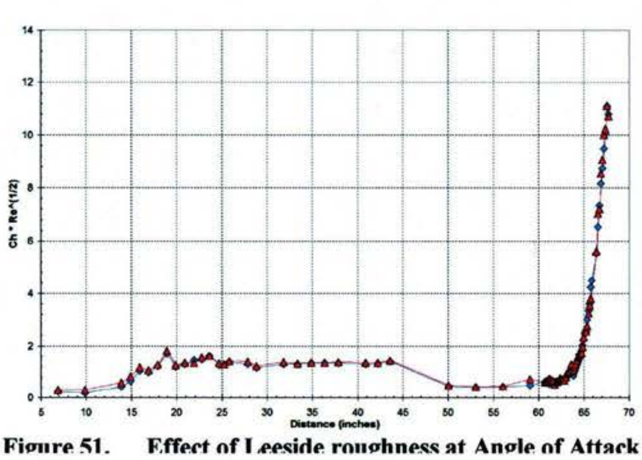

Figure 51. **Effect of Leeside roughness at Angle of Attack**

D. Correlation of Thin-film Transition Results with High-Speed Schlieren Movie Stills

A feature of employing thin-film heat flux instrumentation in the transition region on the cone surface is the ability to follow the transition process from laminar to turbulent. The transition process, based on testing experience at CUBRC over the last 50 years, has been observed to be of two types. The first type can be described as "fingers" of transition that appear to move up and down stream over time and make up the transition front. The second type can be described as regions of turbulence bursting out and moving downstream. Other turbulent bursts break out downstream and coalesce with the upstream bursts until the entire region is fully turbulent.

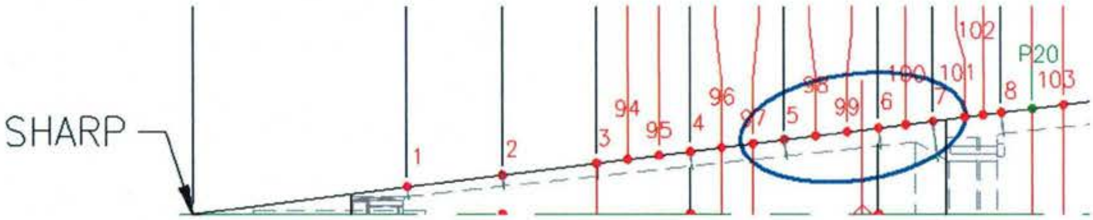

Figure 52. Instrumentation Region of Interest for Schlieren Comparisons

During the HIFiRE ground test program detailed high-speed schlieren videos were taken of the transition region on the cone and these videos have been compared to the thin-film sensors in the same region. Figure 52 shows the instrumentation layout of the HIFiRE model with the circled region showing the instruments that will be compared directly to the schlieren video. Three separate snapshots in time will be presented each showing a different part of the transition process as it occurs on HIFiRE at flight conditions. The first time, Figure 53, shown in the schlieren still (upper right) is represented in the heat flux time history traces by a vertical blue line. These time history traces are compared to locations in the schlieren still with corresponding numbers. Each time history trace represents regions of laminar flow and turbulent bursts that make up the transition region. A closer look at the schlieren still shows laminar flow upstream, transition in the center, and the start of fully turbulent flow downstream. The same state can be seen in the time history traces; time history traces 1. and 2. show laminar flow at this time while 3. and 4. show heat flux approaching turbulent levels. Figure 54 catches a turbulent burst in the

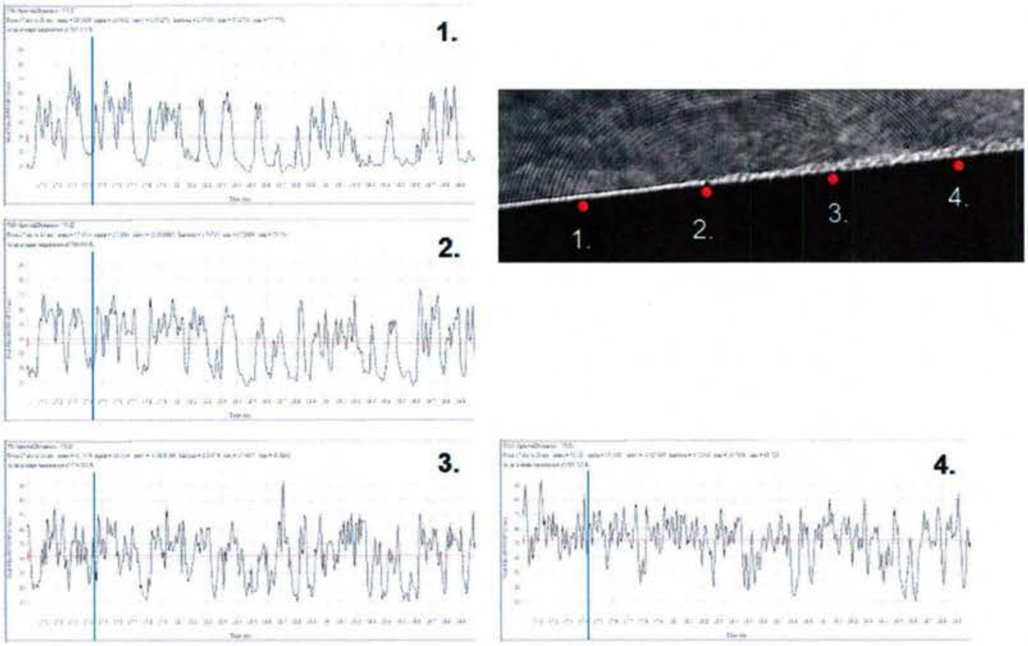

Figure 53. Schlieren Video Still Frame with Corresponding Time History Trance Showing Transition from Laminar to Turbulent Flow

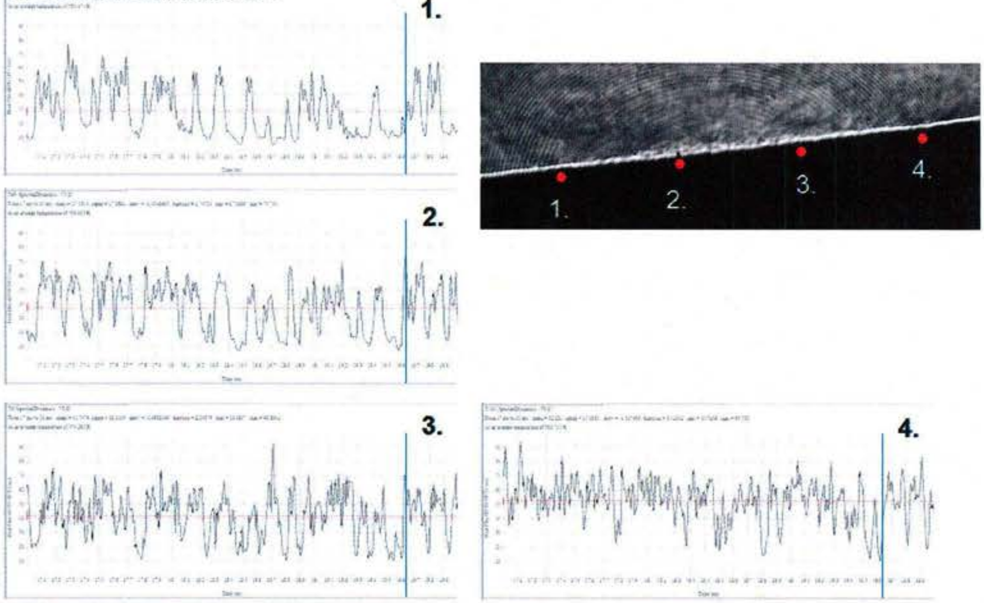

Figure 54. **Schlieren Video Still Frame with Corresponding Time History Trance Showing a Turbulent Burst in the Center of the Window**

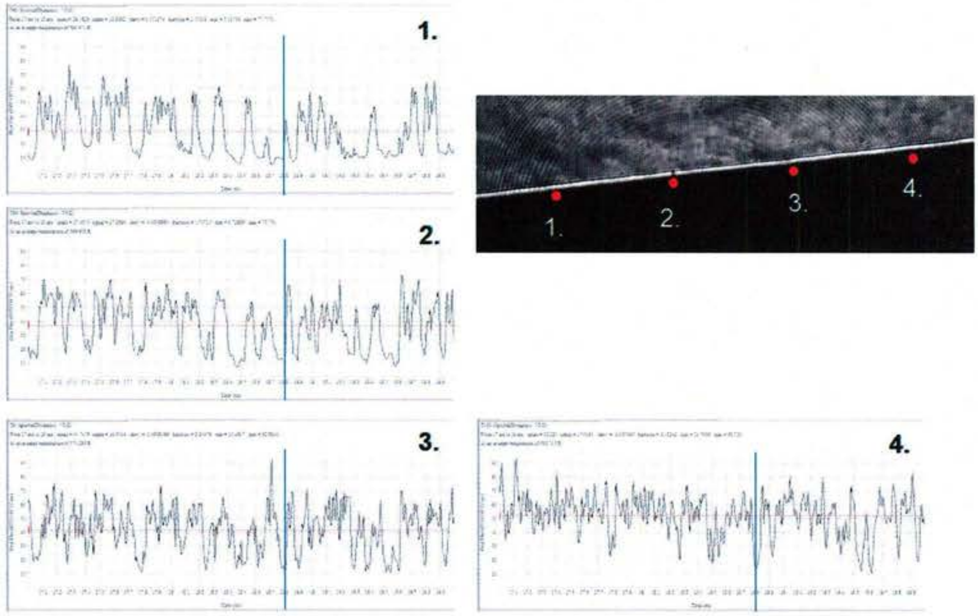

Figure 55. **Schlieren Video Still Frame with Corresponding Time History Trance Showing Laminar Flow Across the Window**

center of the schlieren window and here time history traces 2. and 3. show turbulent levels while 1. and 4. show levels approaching laminar. Finally, Figure 55 shows a state where the entire schlieren window appears to be laminar and again this is born out by the time history traces each showing laminar levels at this time. These figures show the importance of having adequate test time when analyzing the transition process.

E. Measurement of Freestream Fluctuating Pressure Levels

An important component to the assessment of transition in the ground test facility is understanding the level of pressure fluctuation present in the freestream and how it influences the transition mode on the surface of the model. To this end two time of arrival pressure transducers and specially constructed pitot pressure were employed. The time of arrival pressure transducers have been reported in other studies to be capable of measuring the second mode transition frequencies on the surface of the model. These measured frequencies can be calculated and validated with e^N stability codes. These transducers (PCB 132A32) are designed and built by the PCB company to be used to measure the time of arrival of shock and blast waves. They have a very short time constant and specifications state they are capable of measuring frequencies of up to 1 MHz. These transducers were mounted directly to the surface of the cone and acquired data over the entire test program. Figure 56 shows an example of the

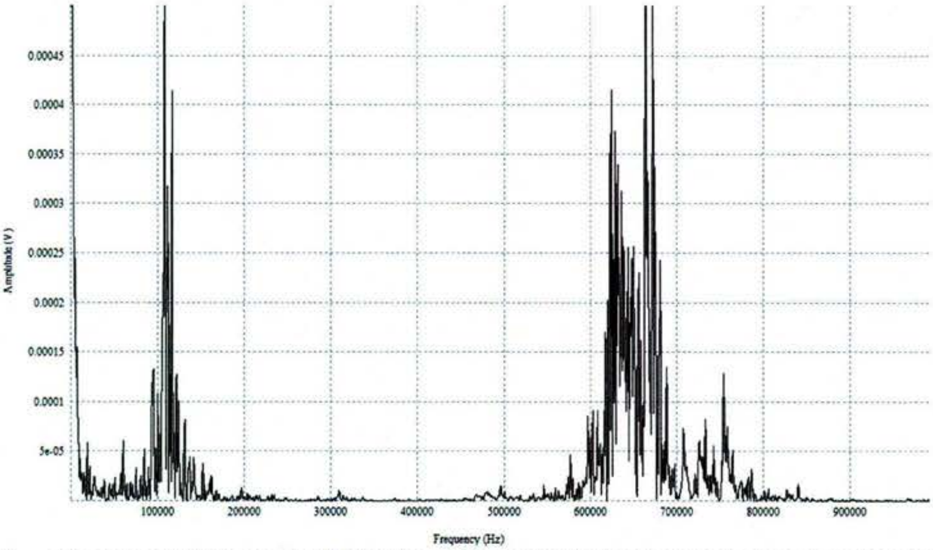

Figure 56. Frequencies Measured with Surface Time of Arrival Pressure Instrumentation at Flight Conditions

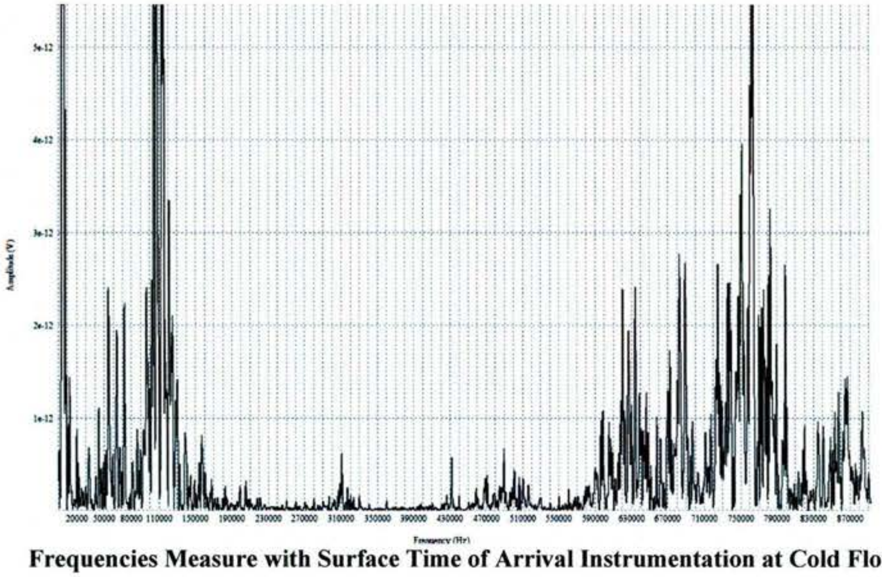

Figure 57. Frequencies Measure with Surface Time of Arrival Instrumentation at Cold Flow Conditions

frequency response from one of the transducers for flight matching test conditions. The large frequency peak at 650 kHz corresponds to the calculated 2nd mode transition frequency output from the STABL code and initially led to the conclusion that the pressure transducers were truly measuring the 2nd mode frequencies. To test this, the freestream velocity condition was varied to be significantly slower and hence drop the 2nd mode transition frequency to a value near 200 kHz. Figure 57 shows the result of this test and unfortunately the same frequencies are present in this case as in the flight velocity case. This issue is still being analyzed at the writing of this paper and additional studies have been planned to further explore measurement of these frequencies.

As mentioned above, pitot pressure measurements were also made to assess the fluctuating pressure component as a percentage of the total pressure that exists in the freestream flow. This fluctuation pressure component originates from the turbulent boundary layer that exists on the wall of the facility nozzle during the test. To obtain this information two different pitot pressure probes were designed. The first was a flush face probe that allowed the pressure transducer sensing surface to be fully exposed to the flow and able to measure the total pressure and the fluctuating component. The second probe was designed to "filter" the fluctuating pressure component out of the measurement by placing the sensing surface of the pressure transducer at the bottom of a cavity inside the probe that is fed by only a small hole in the front face of the probe. The same pressure transducer type, PCB 101A06, was employed in both cases and is capable of measuring up to frequencies of 400 kHz. Figures 58 and 59 show the results of these measurements and after analyzing the RMS values of both signals and getting the difference it can be determined that the fluctuating pressure level for these freestream conditions is between 0.25 and 0.5 percent of the total pressure. Figure 59 is especially encouraging in that the frequencies present in the fluctuating pressure component are much less, 30 to 40 kHz, than the second mode frequency of 650 kHz and should be decoupled from influencing the transition.

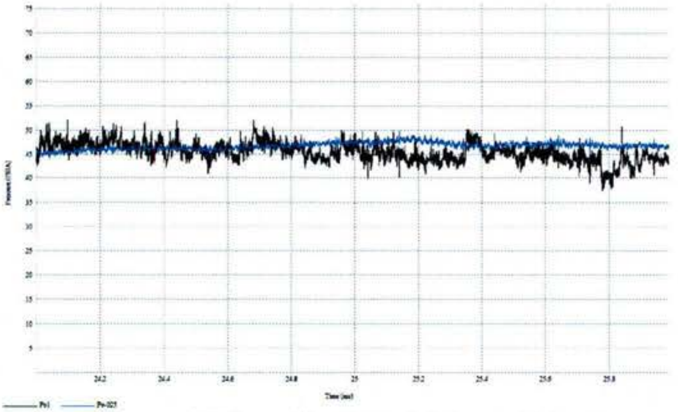

Figure 58. **Time History Traces of "Filtered" and Flush Mounted Pitot Pressure Sensors**

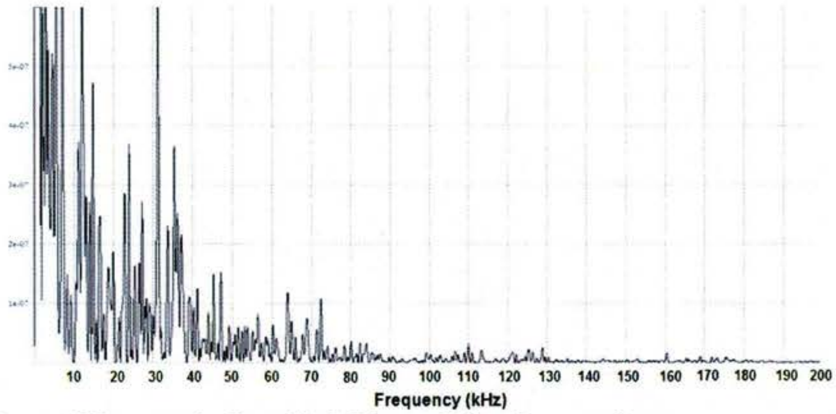

Figure 59. **Measured Frequencies from Flush Mounted Pitot Pressure Senosrs**

V. Computational Results

A. DPLR Navier-Stokes Solver

All ground test studies in the LENS facilities are extensively calibrated and validated with numerical tools. The primary CFD tool used is the DPLR code provided by NASA Ames Research Center. DPLR is a multi-block, structured, finite-volume code that solves the reacting Navier-Stokes equations including finite rate chemistry and finite rate vibrational non-equilibrium effects. This code is based on the data-parallel line relaxation method [Wright 1998] and implements a modified (low dissipation) Steger-Warming flux splitting approach [MacCormack 1989] for the convection terms and central differencing for the diffusion terms. Finite rate vibrational relaxation is modeled via a simple harmonic oscillator vibrational degree of freedom [Candler 1995] using the Landau-Teller model [Landau 1936] Vibrational energy relaxation rates are computed by default from the semi-empirical expression due to Millikan and White [Millikan 1963], but rates from the work of Camac [Camac 1964] and Park, et al [Park 1994] are substituted for specific collisions where experimental data exists. Vibration-dissociation coupling is currently modeled using the T-T_v approach of Park [Park 1987] or with some preliminary implementation of CVDV coupling [Marrone 1963]. Transport properties are appropriately modeled in DPLR for high enthalpy flow [Palmer 2003, Palmer 2003] using the binary collision-integral based mixing rules from Gupta, et al [Gupta 1990]. Diffusion coefficients are modeled using the self-consistent effective binary diffusion (SCEBD) method [Ramshaw 1990]. Turbulence models available in the DPLR code currently include the Baldwin-Lomax 0-equation model [Baldwin 1978], the Spalart-Allmaras model 1-equation model [Spalart 1992], and the Shear Stress Transport (SST) 2-equation model [Menter 1994] each with corrections for compressibility effects [Brown 2002, Catris 1998]. Recent relevant capabilities of the DPLR code involve automated grid adaptation to improve solution quality [Saunders 2007].

B. STABL Tool Package/PSE-Chem Solver

The Stability and Transition Analysis for Hypersonic Boundary Layers (STABL) package [Johnson 2000, Johnson 2005, Johnson 2006] is a comprehensive suite of tools that features an integrated two-dimensional/axisymmetric chemically reacting laminar flow solver, equilibrium chemistry solver, parabolized stability solver, post-processor and various supporting tools and scripting wizards integrated into a single, intuitive, Perl-based GUI interface. The CFD and PSE solvers use MPI for efficient parallel processing. STABL is developed at the University of Minnesota (a combination of versions 2.4 and 2.6 were used for these analyses).

The PSE-Chem solver is a primary part of the STABL suite that solves the parabolized stability equations for two-dimensional or axisymmetric flow derived from the Navier-Stokes equations. The PSE equations are developed by modeling instantaneous flow variables with a mean and fluctuating component and subtracting the mean component from the resulting equation set. The result is a system of 2nd order partial differential equations for the disturbances, which are parabolized according to the method of Herbert [Herbert 1991] by assuming that the disturbances are composed of a fast-oscillatory wave part and a slowly-varying shape function. The ellipticity of the wave part is preserved while only the governing equation for the shape function is parabolized. Assuming that initial disturbances are small and making an assumption of "locally-parallel" flow at the starting plane allows sufficient simplification to generate an initial solution for the shape function and complex streamwise wavenumber. These initial solutions may then be marched downstream by integrating the parabolized stability equations.

The PSE analysis generates a prediction for the evolution of an initial disturbance as it moves downstream from its starting point through the mean flowfield. To predict the onset of transition, an experimental correlation is required. PSE-Chem uses the semi-empirical e^N correlation method

C. Comparisons of Laminar DPLR Solutions with Experimental Data

In parallel with the experimental testing CUBRC also performed computational analysis of the pressure and heating levels on both the cone and cylinder areas of the model. The laminar solutions were compared directly to the baseline laminar levels in the experiment prior to transition and were used to help guide the experimental program and add confirmation to the experimental freestream conditions and model data. These laminar solutions would later be imported directly into the STABL code and used in the stability calculations. Examples of laminar comparisons for both test conditions and bluntnesses can be seen in Figures 59-62. These comparisons show excellent agreement in the laminar flow region ahead of transition. These figures also show the excellent agreement between the four rays of the model. The occasional rise in the data near the 60 inch portion of the plots is due to the flare induced separated region and changes from run to run as the flare angle is being modified.

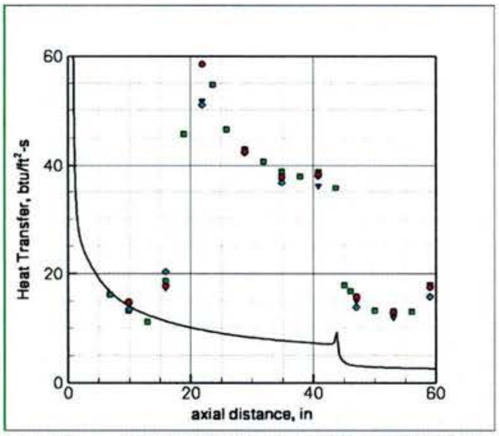

Figure 59. **Mach 6.5 Laminar DPLR Solution of 2.5 mm Nose Case**

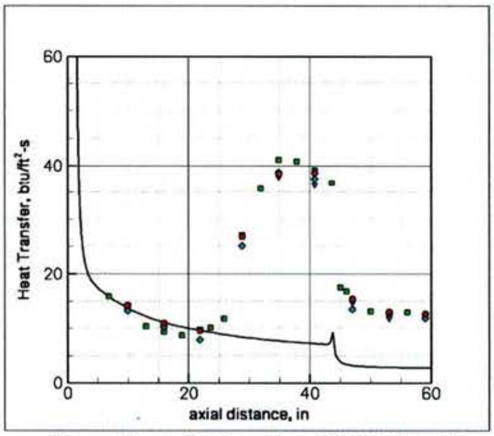

Figure 60. **Mach 6.5 Laminar DPLR Solution of 5.0 mm Nose Case**

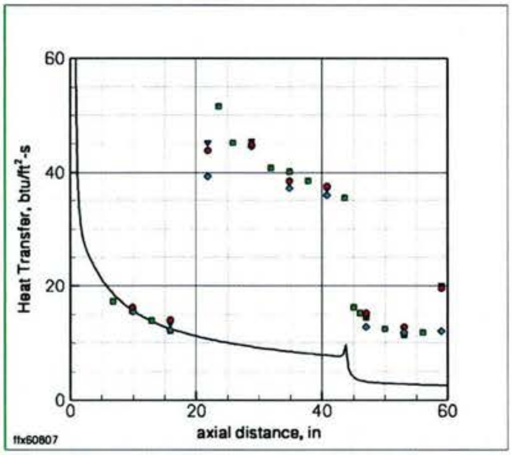

Figure 61. **Mach 7.2 Laminar DPLR Solution of 2.5 mm Nose Case**

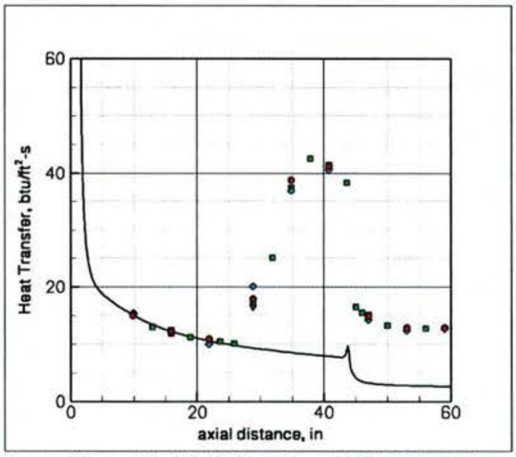

Figure 62. **Mach 7.2 Laminar DPLR Solution of 5.0 mm Nose Case**

D. Employing the DPLR and STABL Codes to Estimate Transition Behavior on Flight Vehicle

The extrapolation of the ground test measurements to flight conditions using the STABL code provided an extremely valuable approach to employing ground test measurements to support the design of flight vehicles. In essence, the measurements made in the ground test environment are employed to calibrate the STABL code, which is then employed to determine the magnitude of the perturbation to transition position for N-factors which have been suggested from flight data. This process is illustrated in Figure 63, where the DPLR code is employed to predict the flow over the blunt cone configuration. The STABL Code solves the parabolized stability equations (PSE) for the growth of first and second mode instabilities by the integration of the disturbance using an e^n fit. Earlier studies have indicated that typical values for N are 5.5 in the wind tunnel and 10 - 11 for flight vehicles. A stability map similar to that shown in Figure 63b is created, which then is employed to plot the n-factor axial distance envelope shown in Figure 63c. An N-factor for the ground test measurements is calculated based upon the measurements of insipient transition and employing flight N-factors of typically 10 one can extrapolate to determine the delay in transition expected for the flight case. Two examples of the extrapolation to flight using this approach are shown in Figure 41a

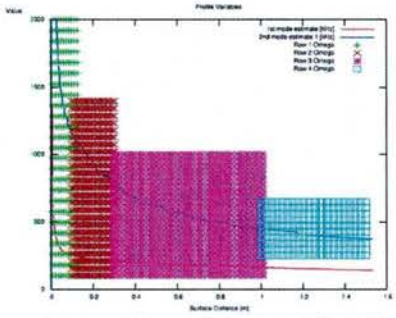

Figure 63a. Calculated Stability Modes

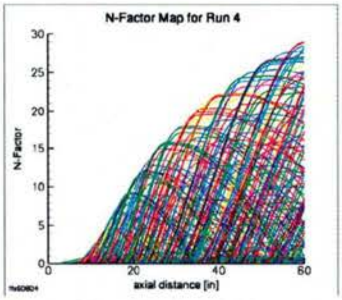

Figure 63b. Typical N-factor Map

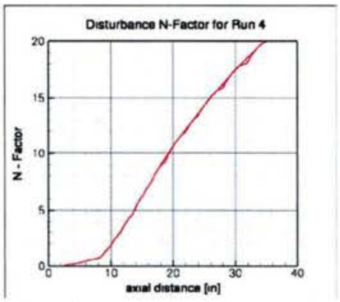

Figure 63c. Maximum N- Factors /Transition Boundary

and b for the Mach number 6.5 and 7.2 test conditions respectively. For the Mach 6.5 condition shown in Figure 64a, this extrapolation technique indicates that transition would move downstream on the cone by approximately 4.5 inches from its measured location at 15 inches. Clearly this is a small increment on the 45-inch cone and would support our conclusion that the model configuration proposed for the flight test was completely acceptable. A similar set of calculations at the 7.2 condition are shown in Figure 64b and again the predicted 10-inch movement of the transition point would not significantly influence our selection of the flight configuration. Additional results were obtained by Johnson at the University of Minnesota employing the same freestream conditions and model geometry [Johnson 2007]. These results are shown in Figure 65. Here an N-factor of 10 moves the transition point moves the transition point downstream by a factor of 5.5 inches; a similar result to the analysis performed by CUBRC.

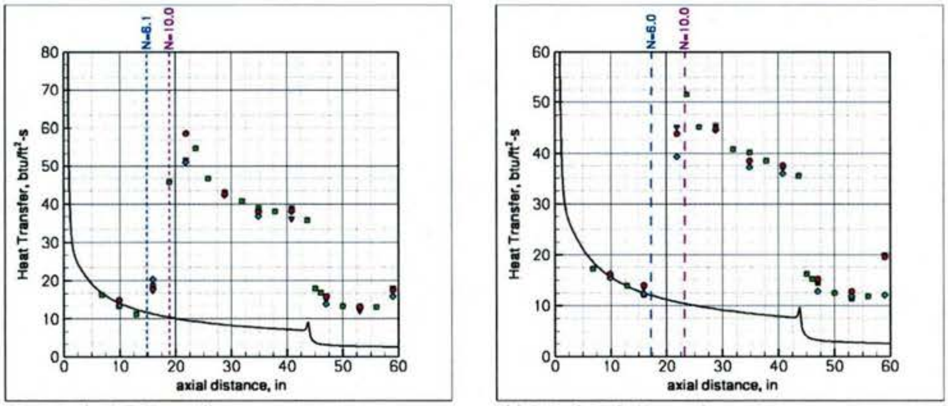

(a) Mach 6.5 (Run 4) (b) Mach 7.2 (Run 5)

- Assuming N_{FLIGHT} = 10 pushes transition back by ~ 4.5"
- This is still further forward than we measured with the larger nose radius (5.0 mm)
- The larger nose radius stayed turbulent beyond the expansion corner, so we conclude that the 2.5 mm radius should produce turbulent flow in the interaction region in flight

Figure 64. Predictions of the Downstream Movement of Transition from Ground Test to Flight

VI.Summary and Conclusions

Experimental studies have been conducted in hypersonic flows to provide measurements with which to evaluate and improve the modeling of turbulence phenomena associated with boundary layer transition and shock wave/boundary layer interaction. These studies were conducted at fully duplicated flight conditions in the LENS I tunnel employing full-scale models of the flight vehicle and components. The studies conducted for the AFOSR-sponsored FRESH FX-1 program were designed to aid in the selection of the configuration to be employed in the

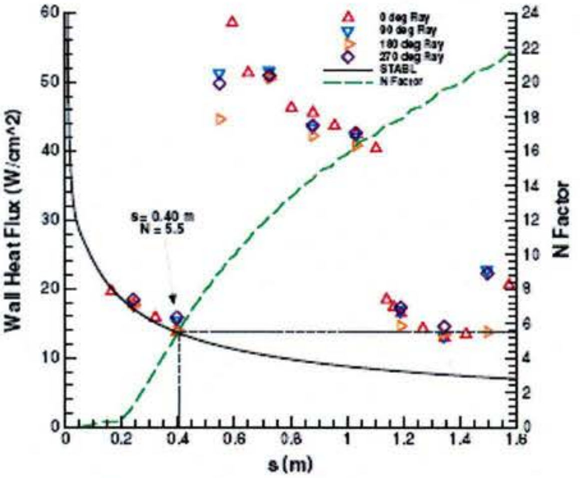

Figure 65. STABL Solution by Johnson Showing Similar Results for the FRESH FX-1 Mach 7.2 Case [Johnson 2007]

flight test program. Schlieren photographs and detailed heat transfer measurements were made to determine the characteristics of regions of boundary layer transition and shock wave/boundary layer interaction over the conical forebody and cylinder/flare section of the models. These measurements, together with numerical computations using the DPLR code, were employed to select a 2.5 mm nosetip radius and a 33° flare angle for the flight vehicle as well as verify that the overall length and geometry of the conical, cylindrical and flare sections of the model would provide valuable data in the flight test program. Flight vehicle geometry selections were further reinforced by stability calculations obtained employing the STABL code that predicted only several inches of down stream movement of the transition point in flight compared to the ground test. Measurements in turbulent flows in these programs gave rise to questions on the selection of the compressible turbulence models used in the numerical calculations. While the measurements were in excellent agreement with laminar DPLR solutions and semi-empirical methods developed over the past three decades, the measurements in fully turbulent regions on the cone section were not well predicted using contemporary turbulence models in the DPLR prediction method. The turbulence modeling will be discussed in detail in AIAA 2008-0641 [MacLean 2008].

VI. Acknowledgments

This work was supported by the Air Force Office of Scientific Research under Grant FA9550-07-1-0486, Subcontract M5146247101. The authors would like to acknowledge the support and guidance of Peter Erbland, Roger Kimmel, and David Adamczak of the Air Force Research Laboratories in Dayton Ohio and John Schmisseur of the Air Force Office of Scientific Research.

VII. References

1). MacLean, M.; Wadhams, T.; and Holden, M. "A Computational Analysis of Ground Test Studies of the HIFiRE-1 Transition Experiment". AIAA Paper 2008 – 0641. 46TH Aerospace Sciences Meeting & Exhibit. Reno, NV: 7-10 January 2008.

2). AAEC Research Staff, "LENS Brochure", *Capabilities and Technologies*, Buffalo, NY 2004

3). Estorf, M., Radespiel, R, Schneider, S., Johnson, H., Hein, S., "Surface-Pressure Measurements of Second-Mode Instability in Quiet Hypersonic Flow". AIAA Paper 2008 – 0641. 46TH Aerospace Sciences Meeting & Exhibit. Reno, NV: 7-10 January 2008.

4). Kimmel, R.; Adamczak, D.; Gaitonde, D.; Rougeux, A.; and Hayes, J. "HIFiRE-1 Boundary Layer transition Experiment Design." AIAA Paper 2007-0534. 45^{TH} Aerospace Sciences Meeting & Exhibit. Reno, NV: January 2007.

5). Holden, M.S., "Shock-Wave Turbulent Boundary Layer Interaction in Hypersonic Flow," AIAA Paper No. 72-74, Paper presented at the AIAA 10th Aerospace Sciences Meeting, San Diego, CA 17-19 January 1972.

6). Holden, M.S. and Moselle, J.R., "Theoretical and Experimental Studies of the Shock Wave-Boundary Layer Interaction on Compression Surfaces in Hypersonic Flow," Calspan Report No. AF-2410-A-1, October 1969, also ARL 70-0002, January 1970.

7). Holden, M.S., "A Review of Aerothermal Problems Associated with Hypersonic Flight," AIAA-86-0267, Paper presented at the AIAA 24th Aerospace Sciences Meeting, Reno, Nevada, 6-9 January 1986

8). Wadhams, T.; MacLean, M.; Holden, M.; and Mundy, E. "Pre-flight Ground testing of the Full-scale FRESH FX-1 at Fully Duplicated Flight Conditions," AIAA Paper 2007–4488. 37^{TH} AIAA Fluid Dynamics Conference & Exhibit. Miami, FL: 25 – 28 June 2007.

9). Van Driest, E., R., "Turbulent Boundary Layer in Compressible Fluids", *Journal of the Aeronautical Sciences*, Volume 18, Pages 145-160, March 1951

10). Cheng, H.K.; Hall, Gordon; Gollian, T.C.; and Hertzberg, A., "Boundary-Layer Displacement and Leading-Edge Bluntness Effects in High-Temperature Hypersonic Flow", Journal of Aerospace Sciences, Volume 28, Pages 353-381, May 1961.

11). Wright, M.J.; Bose, D.; and Candler, G.V. "A Data Parallel Line Relaxation Method for the Navier-Stokes Equations". *AIAA Journal*. Vol 36, no 9. Pgs 1603 – 1609. Sept 1998.

12). MacCormack, R.W. and Candler, G.V. "The Solution of the Navier-Stokes Equations Using Gauss-Seidel Line Relaxation". *Computers and Fluids*. Vol 17, No 1. Pgs 135 – 150. 1989.

13). Candler, G.V. "Chemistry of External Flows". *Aerothermochemistry for Hypersonic Technology*: Von Karman Institute for Fluid Dynamics Lecture Series. VKI LS 1995-04.

14). Landau, L. and Teller, E. "Theory of Sound Dispersion". *Physikalische Zeitschrift der Sowjetunion*. Vol 10, no 34. 1936.

15). Millikan, R. and White, D. "Systematics of Vibrational Relaxation". *Journal of Chemical Physics*. Vol 39, no 12. Pgs 3209 – 3213. 1963.

16). Camac, M. "CO_2 Relaxation Processes in Shock Waves". *Fundamental Phenomena in Hypersonic Flow*. J.G. Hall Ed. Cornell University Press. Pgs 195 – 215, 1964.

17). Park, C.; Howe, J.T.; Jaffe, R.J.; and Candler, G.V. "Review of Chemical-Kinetic Problems of Future NASA Missions II: Mars Entries". *Journal of Thermophysics and Heat Transfer*. Vol 8, no 1. Pgs 9 – 23. 1994.

18). Park, Chul. "Assessment of Two-temperature Kinetic Model for Ionizing Air". AIAA Paper 87-` 1574. AIAA 22^{ND} Thermophysics Conference. Honolulu, HI: 8-10 June 1987.

19). Marrone, P.V. and Treanor, C.E. "Chemical Relaxation with Preferential Dissociation from Excited Vibrational Levels". *The Physics of Fluids*, Vol 6, no 9. Pgs 1215 – 1221. September 1963.

20). Palmer, G.E. and Wright, M.J. "A Comparison of Methods to Compute High Temperature Gas Viscosity". *Journal of Thermophysics and Heat Transfer*. Vol 17, no 2. Pgs 232 – 239. 2003.

21). Palmer, G.E. and Wright, M.J. "A Comparison of Methods to Compute High Temperature Gas Thermal Conductivity". AIAA Paper 2003-3913. Jun 2003.

22). Gupta, R.; Yos, J.; Thompson, R.; and Lee, K. "A Review of Reaction Rates and Thermodynamic and Transport Properties for an 11-Species Air Model for Chemical and Thermal Nonequilibrium Calculations to 30000 K". NASA RP-1232. August 1990.

23). Ramshaw, J.D. "Self-consistent Effective Binary Diffusion in Multicomponent Gas Mixtures". *Journal of Non-Equilibrium Thermodynamics*. Vol 15, no 3. Pgs 295 – 300. 1990.

24). Baldwin, B.S. and Lomax, H. "Thin Layer Approximation and Algebraic Model for Separated Turbulent Flows". AIAA Paper 78-0257. Huntsville, AL: 1978.

25). Spalart, P.R. and Allmaras S.R. "A One-Equation Turbulence Model for Aerodynamic Flows". AIAA Paper 92-0439. 30TH Aerospace Sciences Meeting & Exhibit. Reno, NV: 6-9 Jan, 1992.

26). Menter, F.R. "Two-Equation Eddy-Viscosity Turbulence Models for Engineering Applications". *AIAA Journal*. Vol 32, no 8. Pgs 1598 – 1605. August 1994.

27). Brown, James. "Turbulence Model Validation for Hypersonic Flow". AIAA Paper 2002-3308. 8TH Thermophysics and Heat Transfer Conference. St. Paul, MN: 24 – 26 Jun 2002.

28). Catris S. and Aupoix B. "Improved Turbulence Models for Compressible Boundary Layers." AIAA Paper 98-2696. 2ND Theoretical Fluid Mechanics Meeting: Albuquerque, NM, June 1998.

29). Saunders, D.; Yoon, S.; and Wright, M. "An Approach to Shock Envelope Grid Tailoring and Its Effect on Reentry Vehicle Solutions," AIAA Paper 2007-0207. 45TH Aerospace Sciences Meeting & Exhibit. Reno, NV: 8-11 January 2007.

30). Johnson, Heath B. *Thermochemical Interactions in Hypersonic Boundary Layer Stability*. Ph.D. Thesis, University of Minnesota, Minneapolis, MN, 2000.

31). Johnson, H. and Candler, G. "Hypersonic Boundary Layer Stability Analysis Using PSE-Chem." AIAA Paper 2005-5023. 35TH AIAA Fluid Dynamics Conference and Exhibit, Toronto, ON. June 2005.

32). Johnson, H. and Candler, G. "Analysis of Laminar-Turbulent Transition in Hypersonic Flight Using PSE-Chem." AIAA Paper 2006-3057. 36TH AIAA Fluid Dynamics Conference and Exhibit, San Francisco, CA. 5 – 8 June 2006.

33). Herbert, T. "Boundary Layer Transition – Analysis and Prediction Revisited." AIAA Paper 91-0737. January, 1991.

34). Johnson, H.; Alba, C.; Candler, G.; MacLean, M.; Wadhams, T.; and Holden, M. "Boundary Layer Stability Analysis to Support the HiFiRE Transition Experiment". AIAA Paper 2007 – 0311. 45TH Aerospace Sciences Meeting & Exhibit. Reno, NV: 8-11 January 2007.